A control system approach to subject specific prospective respiratory motion correction in cardiac MRI

Ian H. Burger

Department of Human Biology

University of Cape Town

Thesis presented for the degree of

Doctor of Philosophy

February 2012

Declaration

A control system approach to subject specific prospective respiratory motion correction in cardiac MRI

I, IAN HAMILTON BURGER, hereby declare that the above thesis is my own unaided work both in concept and execution, and that apart from the normal guidance from my supervisor, I have received no assistance.

The thesis has been presented by me for examination for the degree of Doctor of Philosophy in Medicine in Biomedical Engineering.

_____

Signature

_____

Date

Acknowledgements

I would like to express my sincere gratitude to the following people for their assistance and guidance:

University of Cape Town: First and foremost I would like to thank my supervisor Ernesta Meintjes for her advice, support, encouragement and MRI expertise.

Bruce Spottiswoode,for always making time when his assistance was needed and for his motivation and assistance with sequence programing.

Ali Alhamud, Daniele Auger and Muhammad Saleh for stimulating discussions on MRI topics and advice. The radiographers, Petronella Samuels, Marie-Louise and Nailah Maroof, for their assistance with data collection.

Imperial College London: David Firmin, for welcoming me into his research group. Jennifer Keegen for supervising me for the time spent in London. Sonja Nielles-Vallespin and Peter Gatehouse for their patience, and expert advice and vast knowledge of sequence development. Andrew Scott, Pedro Ferreira and Iain Pierce for their assistance with data acquisition and for making my stay in the UK a very enjoyable one.

University of Stellenbosch: Deon Blaauw and Ruan de Hart for their recommendation regarding Control system development.

A sincere thank you to all the subjects that participated in my studies.

My wife and family for encouragement and support throughout this project.

The following organisations have provided the resources used in this work:

The University of Cape Town, Cape Universities Brain Imaging Centre, and the NIHR Cardiovascular Biomedical Research Unit of Royal Brompton.

Funding was provided by the SA/Norway Research Cooperation Programme, the South African Research Chairs Initiative of the Department of Science and Technology and National Research Foundation of South Africa, Medical Research Council of South Africa. This project was supported by the NIHR Cardiovascular Biomedical Research Unit of Royal Brompton and Harefield NHS Foundation Trust and Imperial College London.

Abstract

A control system approach to subject specific prospective respiratory motion correction in cardiac MRI

Ian H. Burger 10 January 2012

Respiratory motion of the heart is a problem for high-resolution cardiac MRI. Diaphragmatic navigator gating with a 5mm acceptance window is most commonly used to address this but has an inherently low respiratory efficiency that is further compromised by respiratory drift. A novel method is presented that uses data from multiple navigators prior to the imaging segment as input for a control system to predict the diaphragm position throughout the imaging segment and correct the slice position in real time. The subject's breathing rate is determined from a short 30 s pre-scan in order to set the frequency in a cosine model of respiratory motion. Results indicate equal or improved image quality with 100% respiratory efficiency compared to 44% respiratory efficiency for respiratory gating with an acceptance window of 5mm at end expiration. This technique demonstrates successful following of respiratory drift.

The relationship between cardiac and diaphragm displacements is highly variable between subjects. A subject-specific non-linear elliptical affine model has been developed to incorporate the effect of hysteresis in motion correction. This enables subject specific estimation of heart position throughout the imaging segment based on predicted diaphragm positions. The elliptical model was validated using the breathing patterns of eight healthy volunteers and compared to a linear affine model. For the elliptical model, the RMS errors of each transformation component were less than 0.5 mm and were significantly ($p < 0.05$) lower than the linear model. It was shown that the model can be accurately constructed within 25s. Finally, the control system was implemented in a respiratory biofeedback (rBF) system that provides visual feedback to subjects of their breathing by displaying diaphragm positions as the altitude of an aeroplane moving across the screen. Including the control system improved the temporal resolution of the visual feedback, reducing jerky movements produced by the absence of navigator data for about 400 ms during the acquisition window.

Table of Content

List of Figures

List of Tables

1. Chapter 1
Introduction

Respiratory motion presents a major problem in cardiac MRI. Breath holding is a popular way to deal with respiratory motion that is still extensively used today. Images are often acquired over multiple breath holds requiring subjects to repeatedly hold their breath. Repeated breath holds, however, often occur at irregular positions and breath holding is difficult for patients with cardiac disease. Pencil beam navigators positioned through the dome of the right hemi-diaphragm accurately monitor respiratory motion. Both slice following and respiratory gating employ navigators to correct for respiratory motion. Slice following uses the diaphragm position immediately prior to the imaging segment and a constant correction factor that corrects for the difference between the displacement of the heart and the diaphragm to update the slice position at the start of the imaging segment. The slice position, however, becomes temporally more out dated throughout the imaging segment. Respiratory gating only acquires data when the diaphragm position is within a certain predefined window that is usually positioned at end-expiration. Respiratory gating suffers from very low respiratory efficiency, around 40% in clinical practise, leading to long scan times.

The main objective of the present study was to implement a control system that uses data from multiple navigators prior to the imaging segment to predict the motion of the diaphragm throughout the imaging segment in order to update the slice positions in real time thus enabling the gating window to be increased or even eliminated. We also hypothesised that a complete model of the heart's position relative to diaphragm positions could be constructed if a sufficient number of samples of the heart's position and shape are acquired at different times in the respiratory cycle together with their corresponding diaphragm positions.

This thesis includes three independent articles that at the time of submission either have or will be submitted for publication, together with a comprehensive introduction, discussion and conclusion. Due to this thesis style there is necessarily repetition of background material in the separate chapters.

In the first chapter we provide an overview of cardiac physiology and anatomy, cardiac imaging, basic MRI physics, selected topics in cardiac MRI, and a comprehensive review of motion correction in cardiac MRI.

Chapter 2 describes the implementation of the predictor estimator that uses the data from multiple navigators prior to the imaging segment to predict diaphragm positions throughout the imaging segment, which can then be used to prospectively correct the slice position throughout the imaging segment. This technique reduces the effects of respiratory motion in cardiac MR without requiring the subject to hold their breath while simultaneously maximising respiratory efficiency. This chapter has been prepared as a manuscript that will be submitted for publication.

In chapter three a subject specific elliptical non-linear model that describes the relationship between the diaphragm position and the displacement of the heart is presented. The subject specific model can be constructed in a short pre-scan of approximately 25 seconds. This chapter is a manuscript that has been submitted for publication.

Chapter four describes how the control system was applied to respiratory biofeedback to improve the temporal resolution of the visual feedback.

A comprehensive discussion that summarises the main findings of the work, highlights limitations and discusses future work is presented in chapter five.

Chapter six presents the conclusions.

1.1 Background theory

1.1.1 Cardiac Anatomy and Physiology

The cardiovascular system is divided into two halves, the system circuit and the pulmonary circuit, that function in series both starting and ending at the heart. The heart consists of a

pericardium, a sac of dense connective tissue that surrounds the muscular part of the heart as well as the roots of major blood vessels. The base of the pericardium is attached to the central tendon of the diaphragm. The heart itself consists mainly of myocardium with a smooth endocardium layer inside that prevents blood clotting. The heart is bordered by the lungs laterally, the sternum anteriorly and the diaphragm inferiorly.

The heart's primary function is as a pump to circulate oxygenated blood through the body and deoxygenated blood to the lungs. The heart consists of four chambers, two atria and two ventricles. The right atrium receives the blood from the body via the inferior and superior vena cava. The blood is then pumped through the tricuspid valve into the right ventricle, which then pumps the blood through the pulmonary valve to the lung via the pulmonary arteries. The oxygen rich blood returning from the lungs flows into the left atrium through the bicuspid valve which pumps the blood into the left ventricle. The left ventricle returns the oxygenated blood to the body through the aorta (see figure 1.1).

The ventricles are the more muscular chambers since the actual pumping is performed by them. The left ventricle is the bigger of the two and has a thicker myocardium enabling it to pump the blood throughout the body. The atria are much smaller and their function is to collect the blood returning from the body and lungs, only a small portion of the blood needs to be pumped into the ventricles as almost 70% of the blood flows freely into the ventricle during diastole as the tricuspid and mitral valves are open during this time.

The coronary arteries supply oxygenated and nutrient filled blood to the heart muscle. There are two main coronary arteries, the left coronary artery that supplies the anterior part of the left ventricle, and the right coronary artery that supplies the right ventricle and the posterior part of the left ventricle. The main coronary arteries stem from the coronary sinus which is the first branch from the aorta and lie on the surface of the heart. The main coronary arteries branch into small arteries that penetrate the cardiac muscle. Approximately one third of all deaths result from cardiovascular disease (Rosamond, 2008) and for this reason there is an enormous interest in imaging the heart and in particular the coronary arteries to investigate normal functioning and pathologies in a non invasive manner.

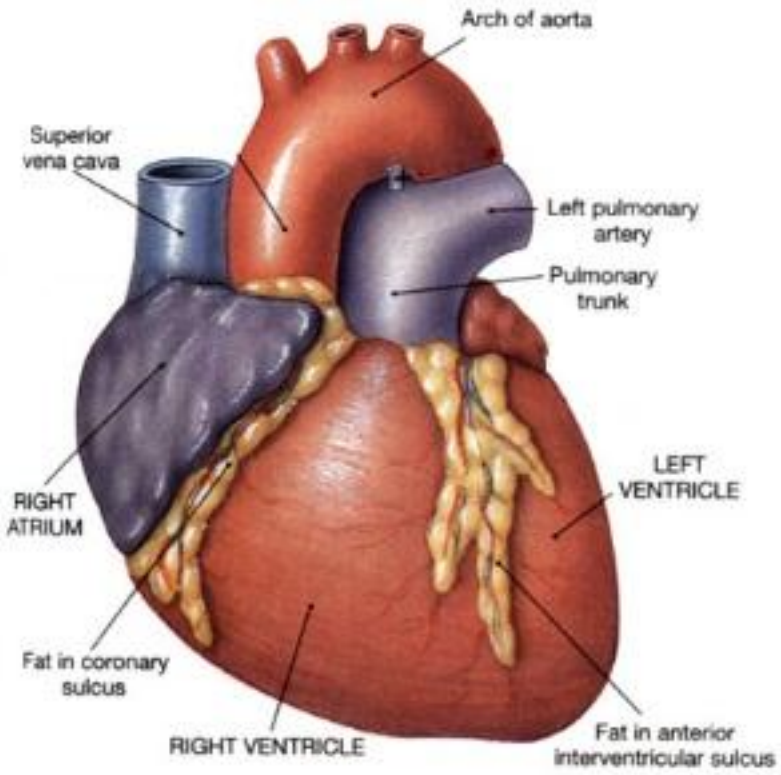

Figure 1.1: Image of the heart showing the ventricles and atria, and the aortic arch and pulmonary trunk. Image adapted from Martini (2007).

The cardiac cycle is defined as the period from the beginning of one heart beat to the next. During this time both the left and right atria and ventricles go through a diastole and systole. The electrocardiogram (ECG) is the measure of the electrical activity generated by the heart and is composed of a P-wave, a QRS complex, and a T-wave for each cardiac cycle, as shown in figure 1.2. The P-wave is caused by depolarisation through the atria which causes the atrial contraction and a rise in the atrial pressure immediately after the P-wave. Approximately 160 milliseconds (ms) later the QRS wave occurs due to the depolarisation of the ventricles causing the ventricles to contract followed by an increase in ventricular pressure. The T-wave is caused by the repolarization of the ventricles and is accompanied by ventricular relaxation at the start of diastole. Total diastole lasts about 200 to 300 ms in a person with a resting heart rate of 72 beats per minute (bpm). During this time the myocardium is relaxed and there is relatively little motion in the heart. Structural imaging of the heart is typically performed during this period of relaxation.

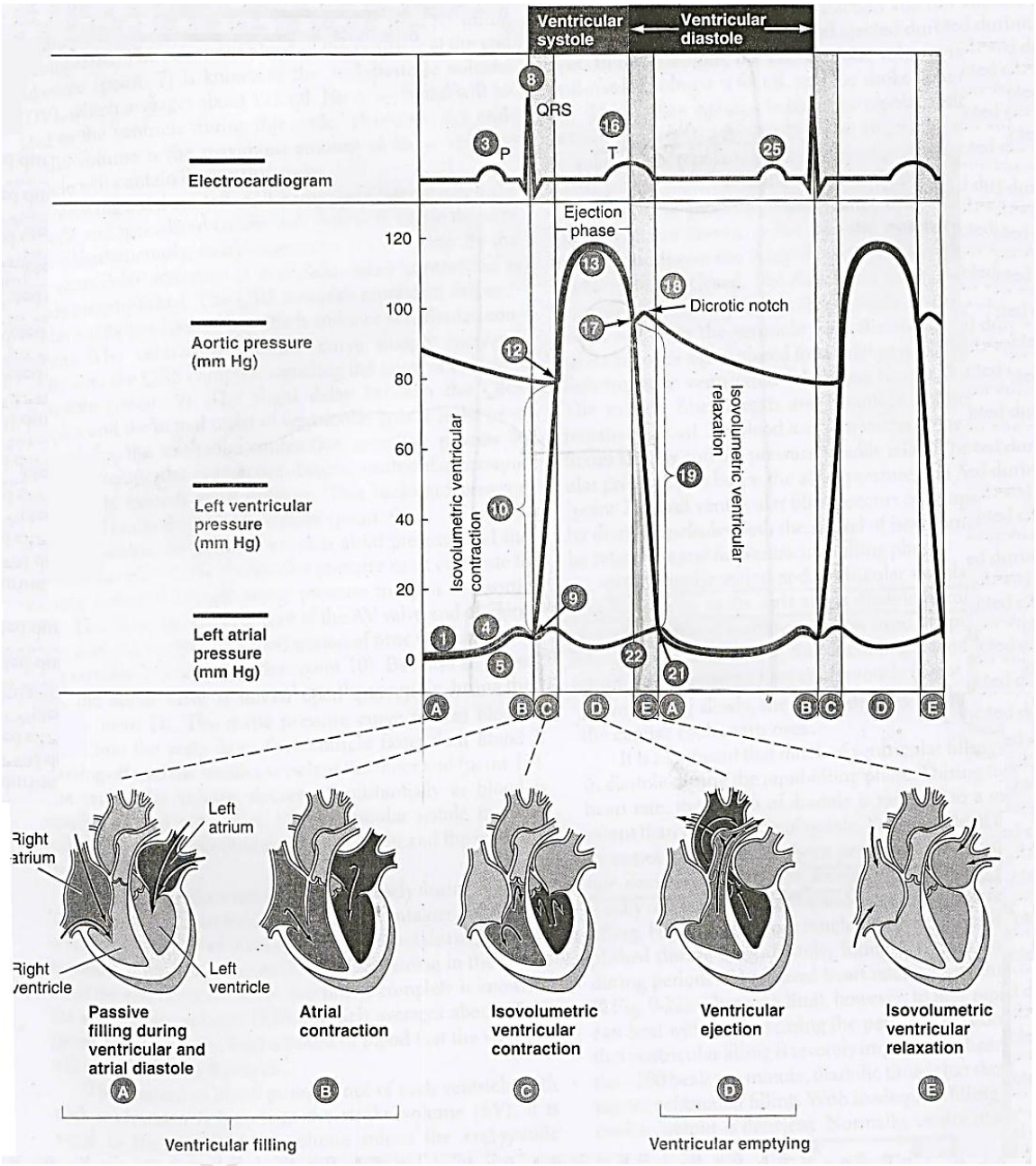

Figure 1.2: The cardiac cycle; electrocardiogram (top), aortic, left ventricular and left atrial pressures (centre), state of the heart (bottom). Image adapted from Martini (2007).

The overall size of the thoracic cavity changes during respiration. During inspiration the diaphragm contracts causing it to flatten, which lowers its dome. The diaphragm is responsible for 60 – 75% of the increase in volume of the thoracic cavity. The rib cage moves up and out, away from the spine producing the remaining 25 – 40% of the volume increase. The external intercostal muscles and interchondral portion of the internal intercostal muscles contract simultaneously causing the ribs to move up and out. Expiration is a passive process during which the muscles of inspiration relax. The ribcage returns to its original position and

the diaphragm pushes up again. The heart undergoes a very complex transformation during respiration. Being attached to the diaphragm the most significant motion is inferior/superior translation. The motion of the ribs causes translation in the anterior-posterior plane as well as the left right direction. This translation is, however, much smaller than that in the superior/inferior direction. The heart also undergoes non-rigid transformation because it is attached to the thorax at various locations. The non-rigid motion consists of shearing, stretching and rotation of the heart in all three planes. In figure 1.3 it can be seen that the thoracic cavity expands most significantly in the inferior direction during inspiration. Further it can be observed that the heart stretches during inspiration.

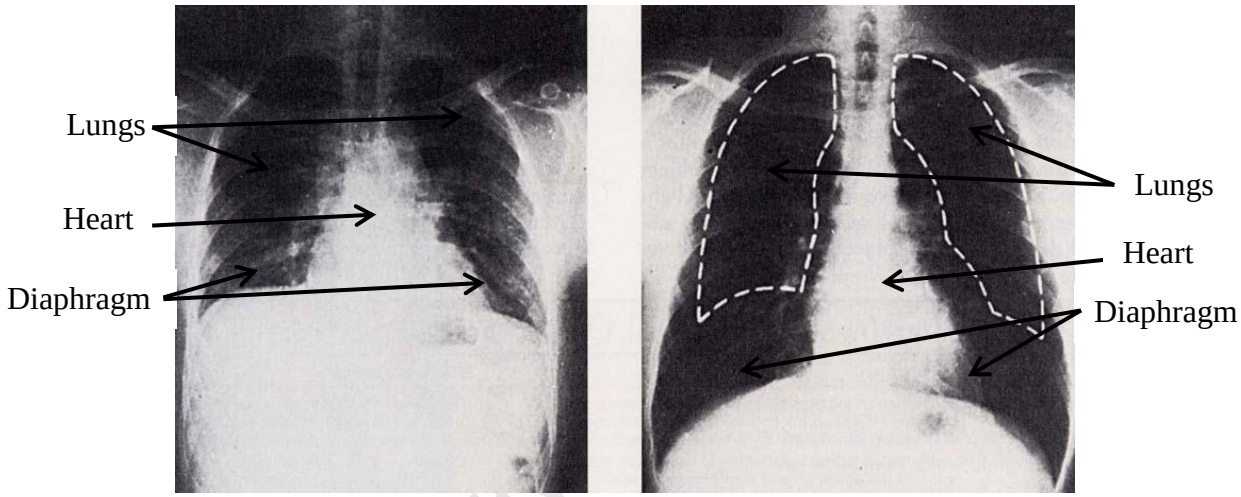

Figure 1.3: Anterior view, x-ray of the thorax at a.) end-expiration and b.) end-inspiration. The images illustrate the change in volume of the thoracic cavity during respiration. The transformation on the heart is also demonstrated. Image adapted from Martini (2007).

During inspiration the intra-thoracic pressure decreases causing blood to flow down the pressure gradient into the lungs and right atrium. The lungs also expand and have a great capacity to hold blood, which will begin to pool there. Baroreceptors in the aortic and carotid sinus will sense a drop in pressure and signal to controllers in the brain to lower inhibition of heart rate via the vagus nerve. (Martini et al., 2007, Shechter et al., 2004)

1.1.2 Cardiac imaging

Cardiovascular disease is the leading cause of death worldwide, accounting for 35.2% of deaths in the United States of America (Rosamond et al., 2008). Non-invasive imaging techniques for the definitive diagnosis and monitoring of cardiovascular disease has greatly altered cardiac imaging in the past 25 years (Higgins, 2000). The three most commonly used

imaging modalities for the diagnosis of heart disease are currently echocardiography, nuclear scintigraphy, and X-ray angiography.

Echocardiography is heavily utilised because of low costs accessibility. It provides high frame rare (200Hz) and is used to characterise cardiac function (volume measurement and wall motion) as well as flow including jets, e.g. for valve assessment. For some patients, the ultrasound (US) window is poor and transesophegal US is used.

Nuclear scintigraphy involves infusing a radioactive compound, or tracer, into the patient. This compound collects in areas of the heart with good blood flow. Gamma rays emitted by the compound are detected using a scintillation camera. Heart-wall movement and overall heart function can be evaluated with cardiac gating. Despite being an excellent tool for functional analysis, morphological detail is limited by the relatively low spatial resolution of nuclear scintigraphy. Nuclear scintigraphy does not provide information on blood flow but on perfusion instead.

X-ray angiography has for decades served as the definitive technique for demonstrating the morphology of a variety of heart diseases. It is also the gold standard for imaging anatomy and pathology of the coronary arteries. A catheter is inserted into a femoral vessel and guided to the heart. An iodinated contrast medium is then injected and its course monitored by acquiring a rapid series of X-rays. X-ray angiography provides both functional and morphological information, but it is very invasive and typically only gives a two-dimensional representation of the three-dimensional process. X-ray angiography (DSA) is the gold standard for assessing coronary arteries. Imaging is limited to projection images, but frequently dual plane setups are used to provide 3D impression.

The ability of Magnetic Resonance Imaging (MRI) to accurately discern soft tissues makes it well suited to studying a range of heart pathologies. In addition to examining soft tissue, MRI also has the ability to obtain images whose signals are proportional to blood flow in vessels, tissue oxygenation, tissue perfusion, mechanical contraction, and the concentration of metabolites in tissues. MRI uses magnetic properties of tissues to create the images instead of radiation which is another big advantage. In cases where contrast is needed, MRI makes use of non-iodine-based contrast agents, since these are known to cause allergic reactions. The one disadvantage of MRI is that it is a relatively slow imaging modality, where single image acquisition times range from hundreds of milliseconds to minutes. The total exam time also takes very long because of the many slow sequences that are usually part of the

comprehensive exam. It is the gold standard for assessment of cardiac function (cardiac output, ejection fraction, myocardial mass, systole volume, diastole volume) and for viability (delayed enhancement imaging).

1.1.3 MRI physics

MRI physics and the Bloch equation

Atoms with an uneven number of nucleons (protons and neutrons) possess a nuclear spin angular moment as well as a magnetic dipole moment given by:

$$\boldsymbol{\mu} = \gamma \boldsymbol{I} \text{ ,} \tag{1.1}$$

where γ is the gyromagnetic ratio, a fixed constant, unique for each nucleus, $\boldsymbol{I}$ is the intrinsic angular moment vector of the nucleus. The hydrogen nucleus, or 'proton', is an example of such a nucleus and is of interest in MRI, because the abundance of hydrogen in water is 63% and its natural abundance is 99.985%.

According to the nuclear Zeeman relationship the energy of the magnetic moment of a nuclear spin in a magnetic field is given by:

$$H = -\boldsymbol{\mu} \cdot \boldsymbol{B_0}\text{,} \tag{1.2}$$

where *H* is the potential energy of the magnetic dipole in a static magnetic field $\boldsymbol{B_0}$. The equation of motion of the magnetic dipole moment in a magnetic field is given by

$$\frac{d\boldsymbol{\mu}}{dt} = \boldsymbol{\mu} \times \gamma \boldsymbol{B_0} \tag{1.3}$$

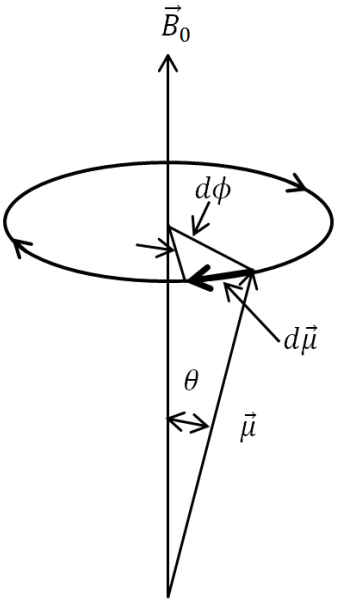

Figure 1.4: Magnetic moment μ in a static magnetic field B_0.

The magnetic dipole moment experiences a torque $\boldsymbol{\mu}\times\boldsymbol{B_0}$ which causes $\boldsymbol{\mu}$ to precess about $\boldsymbol{B_0}$ at the Larmor frequency given by:

$$f_L = \frac{\gamma}{2\pi} B_0 \tag{1.4}$$

or

$$\omega_L = \gamma B_0, \tag{1.5}$$

which is related to the field strength by γ. This relationship assumes that the spins only interact with $\boldsymbol{B_0}$. In reality the spins will interact with each other and with their local environment. According to the classic model of MRI the magnetisation vector $\boldsymbol{M}$ is comprised of three components M_x, M_y and M_z. Bloch suggested that a collection of spins can be viewed, macroscopically, as a net nuclear magnetisation $\boldsymbol{M}$.

$$\vec{\boldsymbol{M}} = \vec{M}_x\boldsymbol{i} + \vec{M}_y\boldsymbol{j} + \vec{M}_z\boldsymbol{k} = \sum_i^N \vec{\boldsymbol{\mu}}_i \tag{1.6}$$

Equation 1.3 can thus be rewritten as:

$$\frac{d\boldsymbol{M}}{dt} = \gamma(\boldsymbol{M}\times\boldsymbol{H}). \tag{1.7}$$

A radiofrequency (rf) pulse ($\boldsymbol{B_1}$) transmitted perpendicular to the main magnetic field at the Larmor frequency ω_L will excite the magnetisation. This is known as the magnetic resonance phenomena. The spins will then absorb energy and rotate out of equilibrium into the transverse plane with an angle, α, which is determined by the magnitude and duration of the rf pulse. Once the rf pulse is turned off, the energy is released as the spins return to the equilibrium state. Bloch described the loss of energy with the following equations:

$$\frac{dM_z}{dt} = \frac{M_0 - M_z}{T1} \tag{1.8}$$

$$\frac{dM_y}{dt} = \frac{M_y}{T2} \tag{1.9}$$

$$\frac{dM_x}{dt} = \frac{M_x}{T2}, \tag{1.10}$$

where *T1* is the longitudinal relaxation time defined by the return of magnetisation to 63% of its maximum value M_0 and depends on the interaction of the spins with the lattice; *T2* the transverse relaxation time defined as the time taken for 63% of the transverse magnetisation M_{xy} to decay due to a loss of phase coherence of the dipole moments.

Equation 1.7 combined with the relaxation described in equations 1.8 to 1.10, yields the Bloch equations:

$$\frac{dM_z}{dt} = \gamma(\boldsymbol{M} \times \boldsymbol{H})_z + \frac{(M_0 - M_z)}{T1} \tag{1.11}$$

$$\frac{dM_y}{dt} = \gamma(\boldsymbol{M} \times \boldsymbol{H})_y + \frac{M_y}{T2} \tag{1.12}$$

$$\frac{dM_x}{dt} = \gamma(\boldsymbol{M} \times \boldsymbol{H})_x + \frac{M_x}{T2} \tag{1.13}$$

MR image acquisition

In MRI one coil is typically used to transmit the rf pulse and another to receiving to detect the signal produced by the relaxing spins. Spatial encoding performed before and during signal acquisition, is used to differentiate the contributions to the signal from different regions of the anatomy in order to produce an image. Three linear field gradients (G_x, G_y and G_z) are superimposed on the stationary field $\boldsymbol{B_0}$ during different times during the pulse sequence

effecting small changes in the local magnetic field experienced by spins at different locations in the scanner.

For a transverse slice, the slice encoding gradient G_z is applied perpendicular to the imaging plane during the rf pulse causing the frequency to vary linearly in the z direction. The result is that only the slice of spins experiencing the Larmor frequency is excited. The slice thickness is determined by the strength of the gradient and the bandwidth of the rf pulse.

The frequency encoding gradient G_x encodes frequency along the x direction during signal acquisition. The phase encoding gradient G_y is applied after slice selection and before signal acquisition and encodes the phase distribution along the y axis. The excitation relaxation cycle is repeated for m different phase encodings. If n data points are sampled during frequency encoding for each phase encoding step, the image resolution will be $m \times n$.

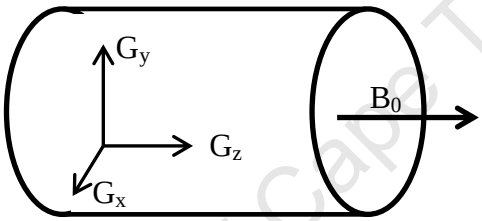

Figure 1.5: The three orthogonal linear field gradients G_x, G_y and G_z, and the static field $\mathbf{B_0}$ in the MRI bore.

The received MRI signal $s_r(t)$ is given by equation (1.14). Contributions from all the precessing transverse magnetisation in the excited slice are included.

$$s_r(t) = \int_{vol} M(\boldsymbol{r}, t)\, dV \tag{1.14}$$

The signal viewed from a reference frame rotating at the Larmor frequency $s(t)$ gives the demodulated baseband signal:

$$s(t) = s_r(t) e^{+i\omega_L t} \tag{1.15}$$

$$s(t) = \int_x \int_y m(x, y) e^{-i2\pi\left[k_x(t)x + k_y(t)y\right]} dx\, dy \tag{1.16}$$

$$s(t) = F_{2D}\{m(x, y)\} \Big|_{\substack{k_{x(t)} = \frac{\gamma}{2\pi}\int_0^t G_x(\tau)\, d\tau \\ k_{y(t)} = \frac{\gamma}{2\pi}\int_0^t G_y(\tau)\, d\tau}} \tag{1.17}$$

and

$$m(x,y) = m_x(x,y) + im_j(x,y). \tag{1.18}$$

In the above equations x and y are space variables and k_x and k_y are spatial frequencies. At any given time the MRI signal $s(t)$ is the two-dimensional Fourier transform of the magnetisation vector $m(x,y)$ at a spatial frequency $\boldsymbol{k}$. By calculating the inverse Fourier transform the value of the magnetisation vector at any location (x,y) can be determined. The two-dimensional Fourier space is referred to as k-space. Each row in k-space represents a frequency encoding step. One row is acquired during each phase encoding step, each time with a different phase encoding gradient resulting in different phase shifts between adjacent columns.

(For more detail on MRI physics refer to Haacke et all., 1999, Hashemi et al., 1997, Spottiswoode, 2006 and Herron, 2008)

1.1.4 Cardiac MRI

Cardiac MRI has many advantages but suffers from slow imaging speed, requiring data acquisition over multiple cardiac cycles. Cardiac triggering makes use of an electrocardiograph (ECG) signal or peripheral monitors to synchronise the pulse sequence to the cardiac cycle of a subject. (Lanzer et al., 1985, Gatehouse and Firmin, 2000). The purpose of cardiac triggering is to minimise motion artifact caused by cardiac motion by acquiring k-space data at the same time point in the cardiac cycle over several cardiac cycles. Cardiac triggering is also used when studying the motion of the heart and several images are acquired at different time points in the cardiac cycle. Steady state free precession (SSFP) or balanced SSFP sequences are typically used for structural cardiac imaging because of their short imaging time. SSFP sequences produce bright blood images with high contrast between the myocardium and the blood within the heart.

Balanced Steady State Free Precession

Steady state free precession is achieved when the net area under the gradient curve on any axis does not vary among the TR intervals. Additionally, if the area under the gradient curve on all axes is zero during each TR interval the peaks of the SSFP-FID and SSFP-echo rephase at the same time TE. The coherent sum of the two signals is the balanced steady state free precession (bSSFP) signal.

The magnitude of the signal depends on whether all the rf excitation pulses have the same phase or are sign alternated. The equation describing SSFP with sign alternation is:

$$bSSFP_{alt} = M_0 sin\theta \frac{1 - E_1}{1 - (E_1 - E_2)cos\theta - E_1 E_2} e^{-\frac{TE}{T_2}} \quad (1.19)$$

and with no sign alternation:

$$bSSFP_{no\ alt} = M_0 sin\theta \frac{1 - E_1}{1 - (E_1 + E_2)cos\theta + E_1 E_2} e^{-\frac{TE}{T_2}}, \quad (1.20)$$

where $E_1 = e^{-\frac{TR}{T_1}}$ and $E_2 = e^{-\frac{TR}{T_2}}$. In practice equation 1.19 is used because the signal is greater than equation 1.20. The sign alternated signal is the same as a pulse sequence with no sign alternation that has a constant precession of the transverse magnetisation by φ = 180 degrees in each TR interval as visualised in figure 1.6 (Hinshaw, 1976).

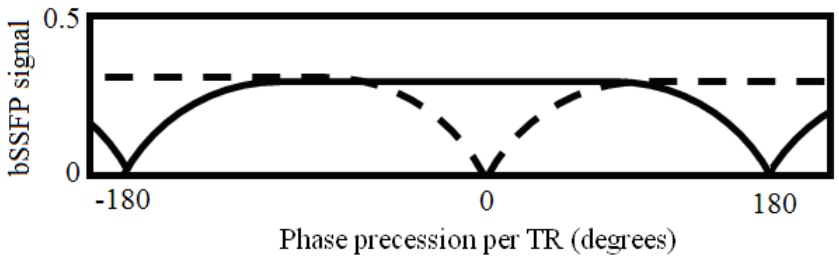

Figure 1.6: Plot of a balanced steady state free precession signal against phase precession φ per TR of the transverse magnetisation. The solid line represents the alternate sign rf pulses, which results in a strong signal on resonance φ = 0 and a minimum at φ =±180. The dashed line represents the rf pulses when the sign is not alternated. The curve is shifted by 180 degrees and the minimum occurs at resonance. The curves repeat with a period of 360 degrees. The shape of the curve depends on T1, T2 and θ.

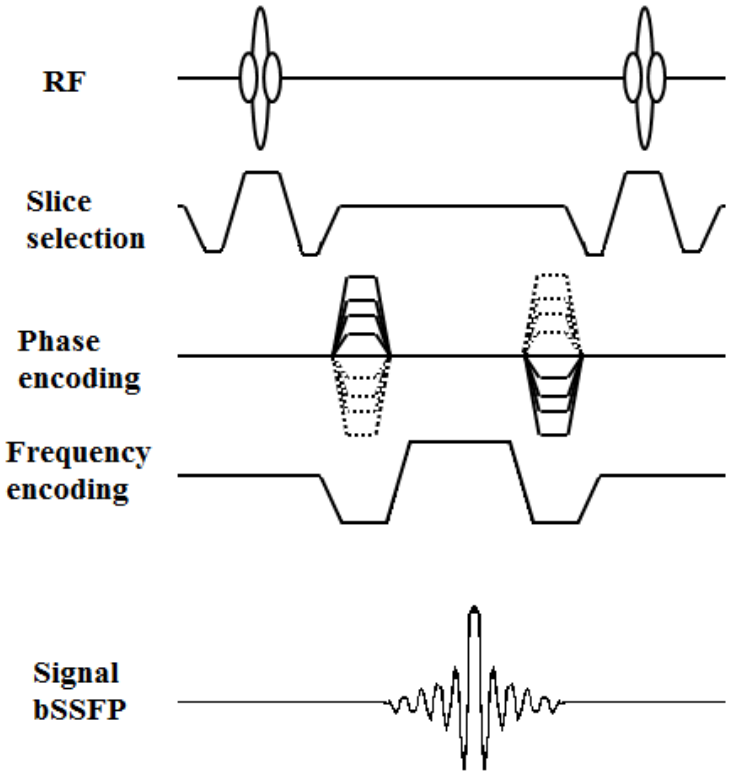

Figure 1.7: Balanced steady state free precession pulse sequence. The net gradient area is zero during one TR interval for any of the three gradient axes.

The bSSFP pulse sequence is displayed in figure 1.7. The bSSFP pulse sequence has a high signal to noise ratio (SNR) and provides T2/T1 contrast weighted contrast, resulting in very bright signal for fluids including blood and fat. The fat signal can be reduced by applying fat saturation pulses or other means such as rf phase cycling. The regions where signal loss occurs due to unwanted phase shifts in the precession angle φ cause bands in bSSPF images. The accumulated phase is proportional to TR. For this reason a short TR is crucial to eliminating banding artifacts. Eddy-current compensation and off resonance shimming can also be introduced to reduce banding artifacts.

Cine MRI

During cine imaging, several images evenly spaced throughout the cardiac cycle are acquired with an cardiac gated fast gradient echo sequence. The images are usually acquired over multiple cardiac cycles and reconstructed to produce a cinematic display of one averaged cardiac cycle. The wall motion of the ventricles and atria, valve motion and the blood flow in the heart and great vessels can be visualised in this way. A cine sequence is also useful to determine the time when the heart goes into diastole for optimum placement of the imaging

window for structural cardiac MR imaging. Figure 1.8 shows 6 evenly spaced images from a cine series of 25 images acquired in a healthy volunteer.

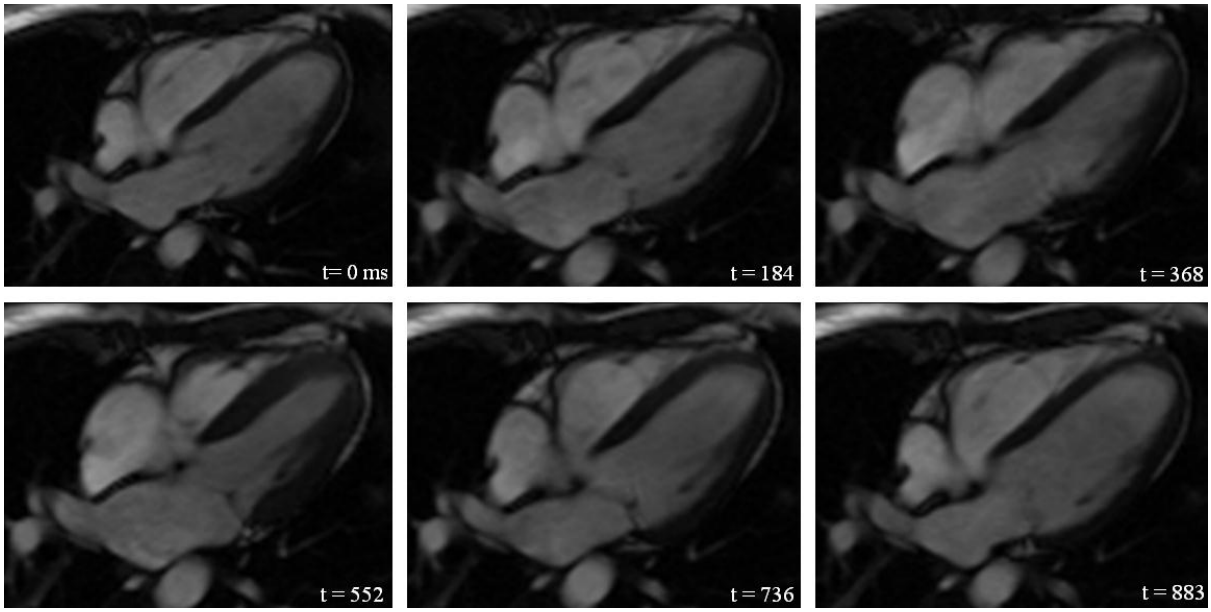

Figure 1.8: Six evenly spaced four chamber view images of a cine series acquired in a healthy volunteer.

Navigators

Patient motion is a problem in all application of MRI. Since chest and heart motion is non-rigid (elastic) it is much more complicated to follow and correct compared to motion in neuro-imaging which is limited to rigid body motion. Navigators rapidly acquire a limited sample of k-space data that is reconstructed to monitor patient motion. One-dimensional navigators are typically used in cardiac MRI, but more complicated designs such as orbital (Fu et al., 1995), clover (van der Kouwe et al., 2006), spherical (Welch et al., 2002), and imaging navigators (White et al., 2010); (Hess et al., 2011) have been developed for other applications, specifically for correction of rigid body motion in neuro-imaging applications.

Navigators are interleaved between data acquisition and motion between the navigator and subsequent acquisition is generally neglected. Navigator data are usually recorded prior to the imaging data acquisition in the same cardiac cycle. Any motion between that navigator and the subsequent image acquisition is usually ignored, which can lead to the acceptance of data that is actually affected by motion. Navigator data may be used prospectively to correct for changes in position that occur during the acquisition or retrospectively to correct for motion during image reconstruction.

In cardiac MRI navigators are usually positioned through the diaphragm to monitor respiratory motion. Two navigator techniques are commonly used for respiratory motion monitoring and correction in cardiac imaging. The first is the spin echo navigator (Ehman and Felmlee, 1989), which uses slice-selective 90 and 180 rf pulses to select the region where two (orthogonal) planes intersect, so that only spins located in a one-dimensional column will contribute to the navigator echo signal as shown in figure 1.9. This navigator is robust but suffers from a slow repeat time in order to avoid saturation effects.

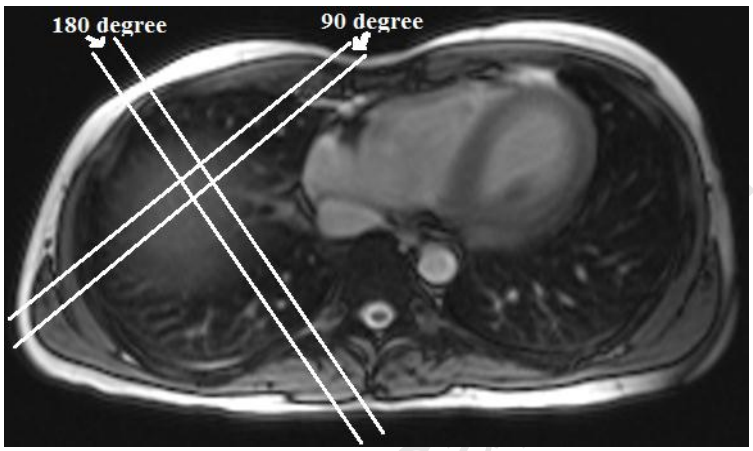

Figure 1.9: Only spins located in the one-dimensional column where the planes excited by the slice-selective 90 and 180 degree pulses intersect will contribute to the navigator signal. The column is positioned over the right hemi diaphragm.

The second is a pencil-beam navigator that uses selective excitation with a two-dimensional spiral gradient. This pulse excites a cylinder in the superior-inferior direction (Pauly et al., 1989). This technique is more susceptible to shimming errors, which can cause blurring, but can be repeated more rapidly since it uses small flip angles.

Figure 1.10 shows an example of data acquired with a navigator positioned through the right hemi diaphragm during free breathing.

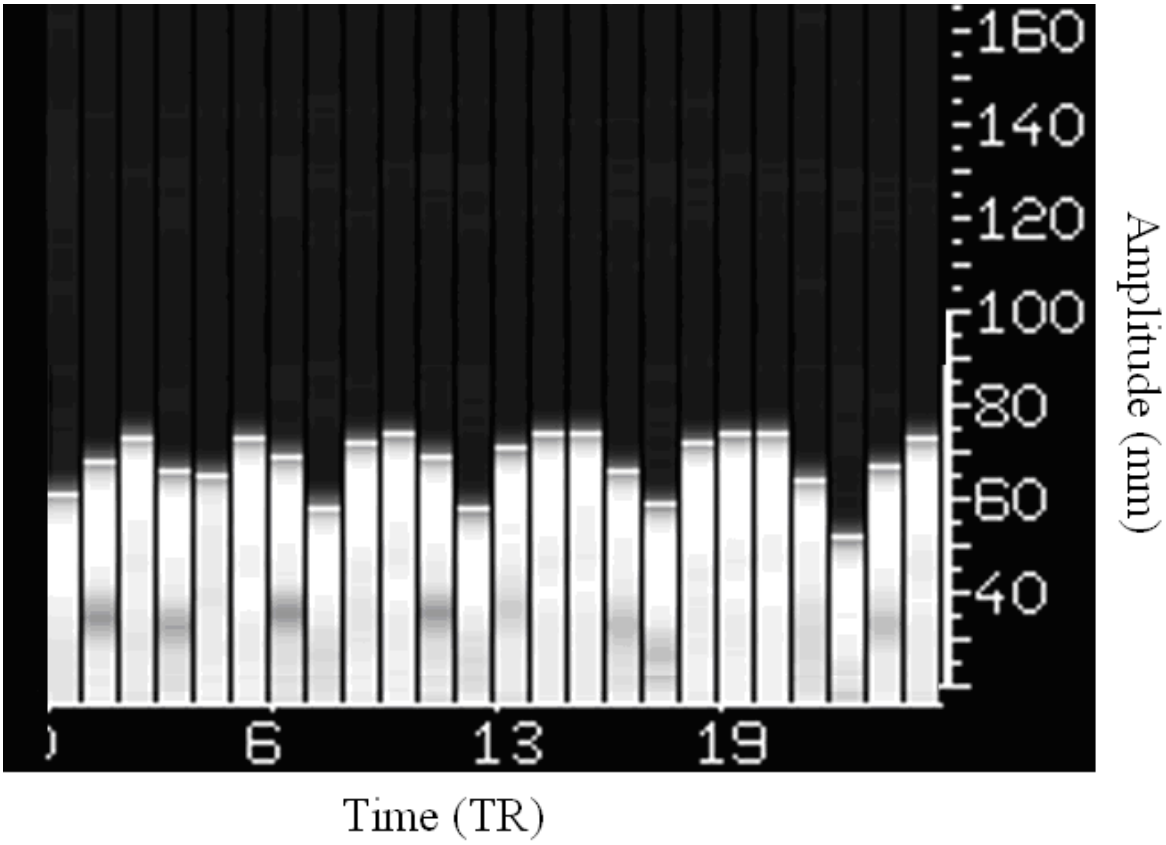

Figure 1.10: Example of navigator data collected through the right hemi diaphragm during free breathing in a healthy volunteer. Each column represents a navigator signal and high signal difference in the column represents the lung/liver interface and is tracked for superior-inferior position of that interface through time.

1.2 Review of respiratory motion correction in cardiac MRI

Cardiac MRI is severely affected by cardiac motion because of the long time needed to acquire images. Cardiac motion can be divided into three categories, motion due to the heart contracting and relaxing throughout the cardiac cycle, respiratory motion, and both voluntary and involuntary motion by the subject (Scott et al., 2009). The latter is mostly managed by patient cooperation, and the former by gating the imaging process using electrocardiogram (ECG) signals and sampling over a number of heart beats. The QRS complex is used as the trigger to indicate the start of a cardiac cycle. This assumes that cardiac motion is the same between heart beats, which is an oversimplification since heart rate and motion vary naturally

(Innes et al., 1993) due to respiration and patient motion. A range of methods have been employed for respiratory motion correction. We present in the following section an overview of these.

1.2.1 Breath hold techniques

Early cardiovascular MR was performed during free breathing with no corrections for the effect of motion on the images (Alfidi et al., 1982, Steiner et al., 1983, Higgins et al., 1985). With the improvement of imaging technology it became possible to complete certain scans within a single breath hold (Atkinson and Edelman, 1991). The problem with this technique is that even healthy volunteers can only hold their breath comfortably for ~ 25-30 seconds (Holland et al., 1998). Since most scans take longer than that to complete, images have to be acquired over multiple breath holds as demonstrated by Feinberg et al. (1995). With advances in cardiovascular MRI to accelerate image acquisition, including amongst others, parallel imaging, non-Cartesian imaging, spatio-temporal correlation (kt-BLAST, compressed sensing) have reduced the scan time of basically all 2D acquisitions to fall within less than 20s. It is the 3D acquisitions that take longer. Some subjects can't hold their breath for even 20s. Janke et al. (2006) have shown in volunteers that subjects hold their breath at irregular positions and that diaphragm positions are unsteady and drift continuously during breath hold (Jahnke et al., 2006). Mcleish et al. (2002) demonstrated that breath hold positions are not within the range of normal breathing, while Holland et al. showed that heart rate increases towards the end of a breath hold (Holland et al., 1998, McLeish et al., 2002). MacCarthy etal. (2003), Danias et al. (1999), and Marks et al. (1997) have extended breath hold duration by supplying oxygen to the subject.

1.2.2 Respiratory Monitoring

Various techniques have been suggested to monitor respiratory motion. Systems that monitor the respiratory motion include belts across the patient chest (Ehman et al., 1984), bellows (Wang et al., 1995a, McConnell et al., 1997) and optical compressing devices (Ehman and Felmlee, 1989). These systems are limited by poor patient cooperation and assumptions about the relationship between device output and heart motion. Navigators rapidly acquire low resolution MR data and use that as guidance for motion detection, monitoring and correction (Bernstein et al., 2005). In cardiac MRI, one-dimensional pencil beam navigators are typically used. The navigator is positioned perpendicular to the edge of the moving structure

(Hinks, 1988). For cardiac MR the navigator is placed across the chest wall, either directly on the heart or the right hemi diaphragm (McConnell et al., 1997, Stuber et al., 1999), the latter being the most commonly used since the contrast between the liver and the lung gives a clear sharp edge. Another advantage of placing the navigator here is that the excited columns do not cross the heart and interfere with the cardiac imaging. The navigator is typically acquired for every cardiac cycle either before, after, or both before and after the imaging segment. The diaphragm position data may be fed back to the patient visually to assist the patient in maintaining a consistent breath hold position (Jhooti et al., 1999). This method relies heavily on patient cooperation and very sick patients are often not able to hold their breath or maintain consistent breath hold positions.

1.2.3 Respiratory gating

Respiratory gating makes use of an acceptance-rejection algorithm (ARA) that is applied during free breathing imaging. The algorithm allows image acquisition if the navigator position falls within a user defined window and rejects it if it doesn't (figure 1.11). While results similar to those obtained with breath hold imaging have been achieved (Sachs et al., 1994, Oshinski et al., 1996), the respiratory efficiency is low because data acquired outside the acceptance window of the cardiac cycle are rejected, leading to long scan times. This method is also susceptible to changes in breathing patterns and respiratory drift (Oshinski et al., 1996). Diaphragmatic navigator gating with a 5mm acceptance window near the diaphragm end-expiratory position (DEEP) is typically used with respiratory efficiency in the order of 40%.

Prospective slice following has been implemented (Danias et al., 1997) to enable larger gating windows and increased respiratory efficiency. This technique uses the navigator position immediately prior to the imaging segment to correct the slice positions throughout the segment. Consequently, the navigator data becomes temporally more out-dated as the segment duration increases and the slice following becomes less accurate.

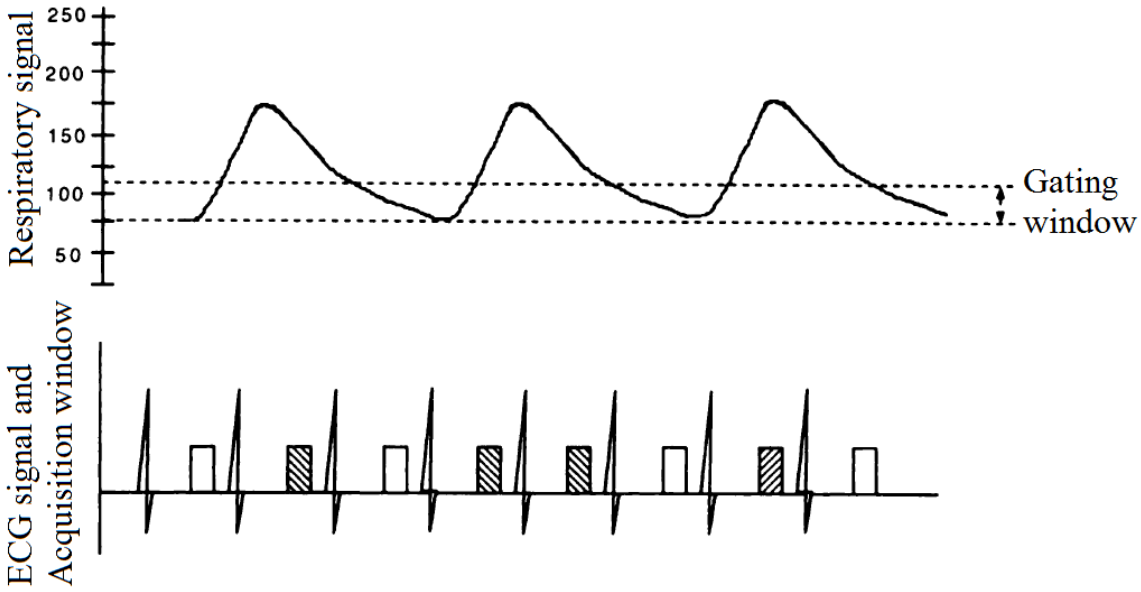

Figure 1.11: Drawing of respiratory gating. Data acquired when the respiratory signal was above the upper window setting, at either the beginning or end of a data acquisition period, were discarded, then data acquisition was repeated until data were acquired when the respiratory signal was below the upper window setting. In this manner, all image data were collected while the respiratory position was within the window shown (expiration). Clear boxes indicate accepted data, and diagonal-striped boxes indicate rejected data. *ECG* = electrocardiographic. Image adapted from Oshinski et al. Radiology (1996). Y-axis in arbitrary units.

Wang and Ehman (2000) and Ehman and Felme (1989) have presented techniques that use navigator data before and immediately following the imaging segment to retrospectively perform correction to enable for larger windows. Using an 8.4 mm window, Wang and Ehman (2000) acquired images with similar resolution to those obtained using an ARA with a 2.8 mm window.

According to Wang et al. (1995), Nehrke et al.(2001), and Taylor (1999) the relationship between the motion of the heart and the inferior-superior motion of the diaphragm is approximately linear (figure 1.12). A correction factor of 0.57 ± 0.26 for right coronary artery (RCA) root and 0.7 ± 0.18 for left anterior descending (LAD) artery corrects for the difference between the diaphragm displacement and the displacement of the heart (Keegan et al., 2001).

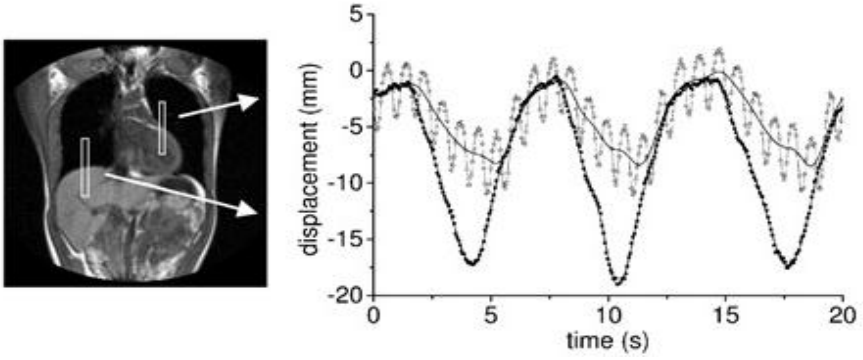

Figure 1.12: Coronal 2D gradient-echo MR image indicates navigator positions (white boxes). Right: Navigator profile images indicate the positions of the heart (thin line) and diaphragm (thick line) as a function of time. The cardiac motion due to the beating heart is superimposed on the navigator profile image of the heart. Image adapted from Nehrke et al. Radiology (2001).

1.2.4 Models of Respiratory motion

Prospective correction techniques enable further widening of the acceptance window. A correction factor is required to compensate for the difference in motion of the heart and the diaphragm. According to Nehrke et al. (2001) the dominant motion of the heart is in the inferior-superior direction with the left-right and anterior-posterior motion significantly smaller. For this reason it is common practice to neglect the smaller components and correct only for the inferior-superior motion. A correction factor of 0.6 has been suggested for coronary imaging. Studies have shown that cardiac motion ranges from 0.22 (range 0.14-0.31) to 0.57+-0.26 of the diaphragm displacement (Wang et al., 1995b, Serfaty et al., 2000).

Studies by Mcleash et al. (2002) and Shechter et al. (2004) have shown that there is significant inter-subject variability in the transformation and rotation of the heart from end-expiration to end-inspiration. Sakuma et al.(2001) found that cardiac blood flow during breath hold at end-expiration is similar to that during free breathing. Schechter et al. (2004) noted that the range of breathing is much smaller during free breathing (around 14 mm) compared to breath hold (up to 40 mm). By doing a short pre scan, subject specific correction factors, or even models of respiratory motion, could be computed and used for prospective motion correction. Previous studies that have modelled the relationship between cardiac and diaphragm motion for prospective motion correction have mostly used breath holding acquisitions to construct the model (Manke et al., 2002a). Their application is limited by the fact that the relationship between the motion of the heart and diaphragm is significantly different during breath hold and free breathing (Serfaty et al., 2000). Methods using multiple

navigators through the heart only sample a few points of the heart (Nehrke and Börnert, 2005). Kozerke et al. adapted the slice offset and angulation according to the motion of the valvular plane of the heart in order to map velocity through the heart valve (Kozerke et al., 1999, Kozerke et al., 2001). Manke et al. performed a study using low resolution 3D images to construct an affine transformation model for subject specific motion (Manke et al., 2002b). Although the results show good following of the heart, the model is linear and as such cannot distinguish between inspiration and expiration, because in a linear model there is only one output for every input. In this application the input is the diaphragm position and the output the displacement of the heart. Nehrke et al. (2001) performed a study tracking the right hemi-diaphragm and left ventricular wall of the heart by placing a navigator over them during free breathing. The results demonstrate significant inter-subject variation and that hysteresis exists in the respiratory pattern. Inspiration and expiration follow different paths and the direction is always counter clockwise (Nehrke et al., 2001).

We know that during expiration the diaphragm pushes up against the heart and this causes an upward translation, craniodorsal rotation and compression of the heart. If, however, we knew exactly what transformation the heart undergoes relative to the diaphragm due to respiration for each subject being scanned prior to image acquisition a much more accurate following could be accomplished that would improve image quality and reduce artifacts. The hysteresis could then also be compensated for by adjusting the correction factor during inspiration and expiration.

We hypothesised that a complete model of the heart's position relative to diaphragm positions can be constructed if a sufficient number of samples of the heart's position and shape are acquired during different times in the respiratory cycle together with their corresponding diaphragm positions.

2. Chapter 2
Control System

2.1 Introduction

Respiratory induced motion of the myocardium presents a major limitation to the quality of cardiac magnetic resonance imaging (MRI). Numerous methods have been implemented to reduce this problem that either require patient cooperation or elongated scan times.

Early cardiovascular MRI was performed during free breathing with no corrections for the effect of motion on the images (Higgins et al., 1985). With the improvement of imaging technology it became possible to complete certain scans within a single breath hold (Atkinson and Edelman, 1991). The problem with this technique is that even healthy volunteers can only hold their breath comfortably for ~ 25-30 s (Holland et al., 1998) which limits the signal-to-noise ratio and resolution achievable. Since most scans take longer than that to complete, images have to be acquired over multiple breath holds. Janke et al. (2006) have shown in volunteers that subjects hold their breath at irregular positions and that diaphragm positions are unsteady and drift continuously during breath hold. Mcleish et al. (2002) demonstrated that breath hold positions are not within the range of normal breathing, while Holland et al. (1998) showed heart rate increases towards the end of a breath hold.

Various techniques have been suggested to monitor respiratory motion. Systems that monitor the respiratory motion include belts across the patient chest, bellows, optical compressing devices, and navigators (Scott et al., 2009). These systems are limited by poor patient cooperation and assumptions about the relationship between device output and heart motion. Navigators use MR data for motion detection, monitoring and correction. The most common navigator is a spin echo navigator where a 90-degree radio frequency (rf) pulse excites a

slice, followed by a 180-degree pulse and a frequency encoding gradient applied along the length of the beam/column. The navigator is positioned perpendicular to the edge of the moving structure (Hinks, 1988). For cardiac MRI, the navigator is typically placed either directly on the heart or perpendicular to the right hemi diaphragm, the latter being the most commonly used since the contrast between the liver and the lung gives a clear sharp edge. Another advantage of placing the navigator here is that the navigator artefact (caused by exciting the two intersecting slices) does not cross the heart and interfere with the cardiac imaging. The navigator is typically acquired during every cardiac cycle either before, after, or both before and after the imaging segment. The diaphragm position data may be fed back to the patient visually to assist the patient in maintaining a consistent breath hold position (Liu et al., 1993). This method relies heavily on patient cooperation and very sick patients are often not able to hold their breath or maintain consistent breath hold positions.

Navigator gating uses the acceptance-rejection algorithm (ARA) which is applied during free breathing imaging. The algorithm allows image acquisition if the navigator position falls within a user defined window and rejects it if it does not (Oshinski et al., 1996). While results similar to those obtained with breath hold imaging have been achieved, the respiratory efficiency is low because data acquired outside the acceptance window of the respiratory cycle are rejected, leading to long scan times (Sachs et al., 1994, Oshinski et al., 1996). This method is also susceptible to changes in breathing patterns and respiratory drift (Oshinski et al., 1996). Diaphragmatic navigator gating with a 5 mm acceptance window near the diaphragm end-expiratory position (DEEP) is typically used.

Prospective slice following has been implemented to enable larger gating windows and increased respiratory efficiency (Danias et al., 1997). This technique uses the navigator position immediately prior to the imaging segment to correct the slice positions throughout the segment. Consequently, the navigator data becomes temporally more out-dated as the segment duration increases and the slice following less accurate.

Wang and Ehman (2000) and Ehman and Felmlee (1989) have presented techniques that use navigator data before and immediately following the imaging segment to retrospectively perform correction to enable larger acceptance windows. These techniques assume that the diaphragm position varies linearly through the imaging segment. Using an 8.4 mm window, Wang and Ehman acquired images with similar resolution to those obtained with a 2.8 mm ARA window but with increased respiratory efficiency (Wang and Ehman, 2000).

The relationship between the displacement of the heart and the inferior-superior motion of the diaphragm is approximately linear (Wang et al., 1995b, Nehrke et al., 2001). A correction factor of 0.57 ± 0.26 for right coronary artery (RCA) root and 0.7 ± 0.18 for left anterior descending (LAD) artery is commonly used to correct for the difference between the diaphragm displacement and the displacement of the heart (Wang et al., 1995b).

The present study aims to develop a technique that uses the data from multiple navigators prior to the imaging segment as input data for a predictor estimator control system. The output of the estimator is the predicted diaphragm position throughout the imaging segment which can then be used to implement slice following in real time. This technique aims to reduce the effects of respiratory motion in cardiac MRI without requiring the patient to hold his/her breath, while simultaneously maximising respiratory efficiency.

2.2 Methodology

2.2.1 Control System Theory

A predictor estimator is a control system that compares a model of a plant to sensor readings of the plant and outputs an estimate of the upcoming state of the plant. This control system is called a predictor estimator because a measurement of sample *k* yields an estimate of the state vector for sample *k*+1.The block diagram in figure 2.1 provides a simple layout of the system and how it has been incorporated in the motion correction algorithm.

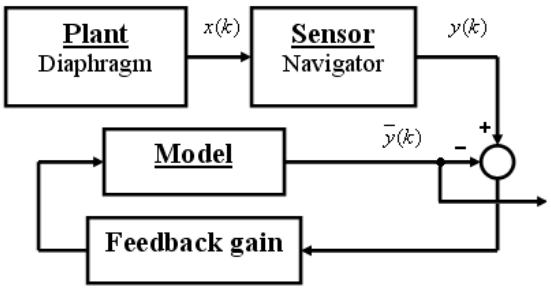

Figure 2.1: A block diagram of the control system, where *x(k)* is the current state of the plant, *y(k)* is the current state of the output vector and $\bar{y}_{(k)}$ is the output vector of the model.

The predictor estimator uses the actual measured states, *y(k)*, for k = 1 to (n-1) to calculate the predicted state, $\bar{x}(k+1)$, with the samples acquired at a fixed sample rate with period T. The method used to estimate the state vector is to construct a model of the plant dynamics, using

$$\bar{x}(k+1) = \Phi\bar{x}(k) + \Gamma u(k), \tag{2.1}$$

$$\bar{y}(k) = H\bar{x}(k), \text{ and} \tag{2.2}$$

$$x = x - \bar{x}, \tag{2.3}$$

where Φ is the discrete state matrix, $\bar{x}(k)$ is the current state of the model, Γ is a constant defined by: $\Gamma = \int_0^T \ell^{F\eta} \cdot G$ and $u(k)$ is the initial state. $\bar{y}(k)$ is the output matrix of the model, $\bar{x}(k+1)$ is the subsequent state of the model, and $\tilde{x}$ is the error. A comprehensive derivation of the equations is given in the appendix. The error is fed back to the model constantly to minimize divergence from the measured signal according to the equation

$$\bar{x}(k+1) = \Phi\bar{x}(k) + L_p[y(k) - H\bar{x}(k)], \tag{2.4}$$

in which Φ and H are the output matrices and L_p is the feedback gain matrix. A large enough L_p ensures sufficiently fast convergence to the plant. When the measured sample is trusted, a large L_p is favourable. If, however, the sensor is unreliable or noisy, it is advised to set L_p to a smaller value that relies more on the model.

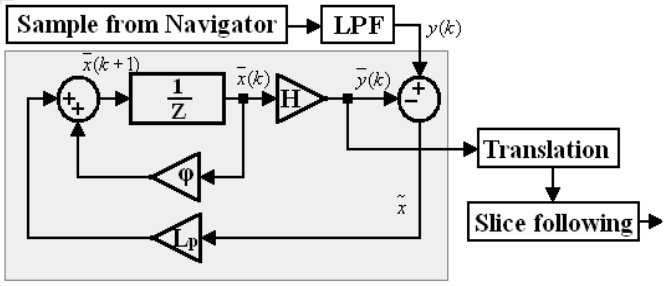

Figure 2.2: Block Diagram of the predictor estimator implemented for diaphragm position prediction, where Φ = the discrete state matrix, $\bar{x}(k)$ = the current state of the model, $\bar{y}(k)$ = the output matrix of the model, $\Gamma = \int_0^T \ell^{F\eta} \cdot G$, and $\bar{x}(k+1)$ = the subsequent state of the model

In a regression analysis of the respiratory traces of 8 healthy volunteers, the control system implemented with a sine wave model explained 95.3% of the variance in the signal. The mathematical model for the system is:

$$f(kT_s) = \sin(akT_s), \tag{2.5}$$

where a is the frequency of the breathing/oscillation and T_s is the sample rate. The discrete state matrix is calculated by first computing the Laplace transform and then the transfer function of $f(kT_s)$. The continuous state matrix is calculated from the transfer function, which is substituted into equation 2.6 to produce the discrete state matrix.

$$\Phi = e^{FT_s} \approx I + (FT_s) + \frac{(FT_s)^2}{2!} + \frac{(FT_s)^3}{3!} \approx I + (FT_s) \tag{2.6}$$

$$\Phi = \begin{bmatrix} 1 & -a^2T \\ T & 1 \end{bmatrix} \tag{2.7}$$

Since the required output is the current state x_1 we set the output matrix to

$$H = \begin{bmatrix} 1 & 0 \end{bmatrix}. \tag{2.8}$$

Next we place the poles, which determine whether the system follows the model or the plant more closely:

$$Z_{est} = placed\ \ poles = real \pm j\ imaginary = Z_{estR} \pm Z_{estI}. \tag{2.9}$$

Factorizing and simplifying gives:

$$Z^2 - Z_{est1}Z + Z_{est2} = 0. \tag{2.10}$$

From control system theory (Franklin et al., 1998) we know that:

$$\left| ZI - \Phi + L_p H \right| = 0. \tag{2.11}$$

Substituting Φ and H into equation 2.11 yields

$$(Z + L_{p1} - 1)(Z - 1) - (L_{p2} - T)(a^2T) = 0. \tag{2.12}$$

Solving for L_p gives:

$$L_p = \begin{bmatrix} L_{p1} \\ L_{p2} \end{bmatrix} \quad , \tag{2.13}$$

where

$$L_{p1} = -Z_{est1} + 2 \tag{2.14}$$

and

$$L_{p2} = \frac{a^2T^2 - Z_{est2} + 1 - L_{p1}}{a^2T} \tag{2.15}$$

The control system was implemented to predict the diaphragm position in order to achieve real time respiratory motion correction in cardiac MRI.

In order to link the terminology used in digital control systems to that used in imaging for the remainder of this document, the plant refers to the diaphragm position, the sensor to the navigators, and the model to the mathematical model defined in equation 2.5 that describes the motion of the diaphragm.

The model was constructed prior to scanning. Since breathing rate varies for individuals, the frequency of breathing was determined from a short period of diaphragm monitoring performed at the start of the scan. The dominant frequency obtained from the Fast Fourier Transform (FFT) of the breathing pattern acquired was used as the model's frequency. The frequency is updated throughout the scan by means of the feedback in order to ensure that the control system remains accurate even if the respiratory rate increases or decreases during the scan.

Since gradient echo sequences are widely used for cardiac MRI, we implemented the control system in the navigator gated balanced steady state free precession sequence (nav-bSSFP).

2.2.2 Sequence Programming

A standard navigator gated balanced steady state free precession (bSSFP) sequence was modified to acquire multiple navigators throughout the cardiac cycle. Samples of the diaphragm position are acquired every 100 ms. Since navigators cannot be applied during the

imaging segment, no data of respiratory motion is available during that time. The navigator is executed repeatedly during the systolic part of the cardiac cycle to acquire data prior to the imaging segment to drive the error (x) to a minimum before starting the imaging segment. This ensures that the model output converges toward the actual diaphragm position (see figure 2.3).

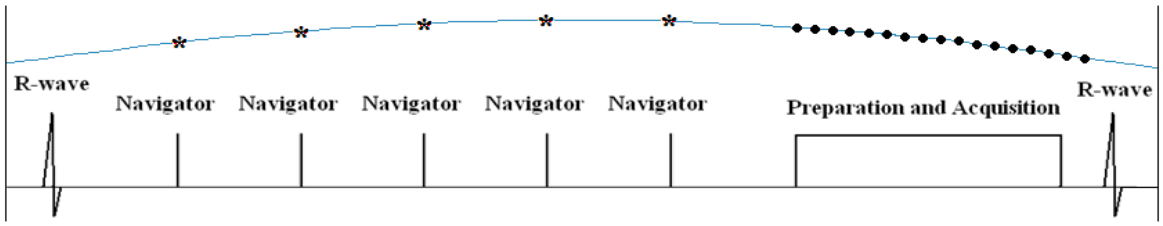

Figure 2.3: A Graph showing a sine wave model of respiratory motion. The *'s denote the navigator readings and the points the output of the control system for the imaging segment of a single cardiac cycle. The duration of the cardiac cycle is 1000ms, the navigator repeat time is 100ms and the acquisition window is 200ms.

During the imaging segment, when no navigator readings are acquired, the system sets the feedback error (x) equal to 0. When the error is zero, equation 2.4 becomes:

$$\bar{x}(k+1) = \Phi\bar{x}(k) \quad . \tag{2.16}$$

This means that the output is equal to the model value $y(k)$ for sample k during the imaging segment. The model is not influenced by the sensor, so that for subsequent samples the output will follow the model. When the imaging segment is completed, the navigator is applied again at the start of the following cardiac cycle, supplying the control system with a new plant measurement.

The spin-echo navigator repeat time is limited by the relaxation time of the excited tissue. Even though it would be ideal to reduce the repeat time to a minimum, the navigator signal becomes noisy if the repeat time is reduced below ~ 100 ms.

A real time low pass filter (LPF) is applied to the navigator signal before it is transmitted to the estimator to reduce high frequency noise. Since breathing is a low frequency signal of the order of 0.1 Hertz, a LPF with a cut off frequency higher than the Nyquist frequency will not alter the actual signal. The base frequency of the respiratory signal is about 0.3Hz, but can vary significantly and is not always steady.

A digital control system functions periodically. This requires each sample interval and cycle duration to be constant and the cycle length to be a multiple of the sample interval so that sampling occurs at the same time during each cycle. In a physiological environment this poses a problem. The control system has been fitted into the sequence without disturbing the timing or influencing the working thereof. The sequence timing is based on the ECG trigger and assumes that each cardiac cycle is approximately the same duration (see figure 2.4).

The period of the control system (T_{nav}) will be equal to the navigator repeat time which is set by the user and is fixed. The duration of the cardiac cycle (T_{cs}) needs to be an exact multiple of this time, which will not be the case. The timing of the control system therefore needs to be adjusted.

The average heart rate of the patient is automatically recorded before the start of the scan once the ECG electrodes are placed and connected to the system. The average duration of the cardiac cycle is saved in the control system as the initial cardiac cycle length ($T_{cs\text{-}init}$). The user is required to provide values for the acquisition window length (T_{awl}) and start time (T_{aws}) on the scanner console.

When the next ECG trigger is received, the time since the previous trigger is calculated and saved as the length of the last cardiac cycle ($T_{cs\text{-}prev}$).

The time between the end of the acquisition window and the start of the subsequent cardiac cycle is T_{dead} and is given by

$$T_{dead} = T_{cs-prev} - (T_{awl} + T_{aws}) \tag{2.17}$$

To calculate how many navigators can be applied per cardiac cycle the following equation is used:

$$\text{Number of navigators (NN)} = \text{integer } (T_{aws} / T_{nav}). \tag{2.18}$$

Since it is optimal to apply the last navigator as close as possible to the imaging segment, we need to calculate the waiting time (T_{wait}) after the ECG trigger before the first navigator should be applied, according to

$$T_{wait} = T_{aws} - (T_{nav} \times NN). \tag{2.19}$$

The time from the last navigator of the current cardiac cycle to the first navigator of the subsequent cardiac cycle is then:

$$T_{extra} = T_{dead} + T_{awl} + T_{wait}. \tag{2.20}$$

Dividing T_{extra} by the period yields the number of samples that can be obtained in the allowed time. The remainder does not fit in and thus we have to add a phase shift to synchronise the control system with the physiological timing.

$$\zeta = T_{extra} \bmod T_{nav} \tag{2.21}$$

$$f(kT_s) = \cos(akT_s + \xi) \tag{2.22}$$

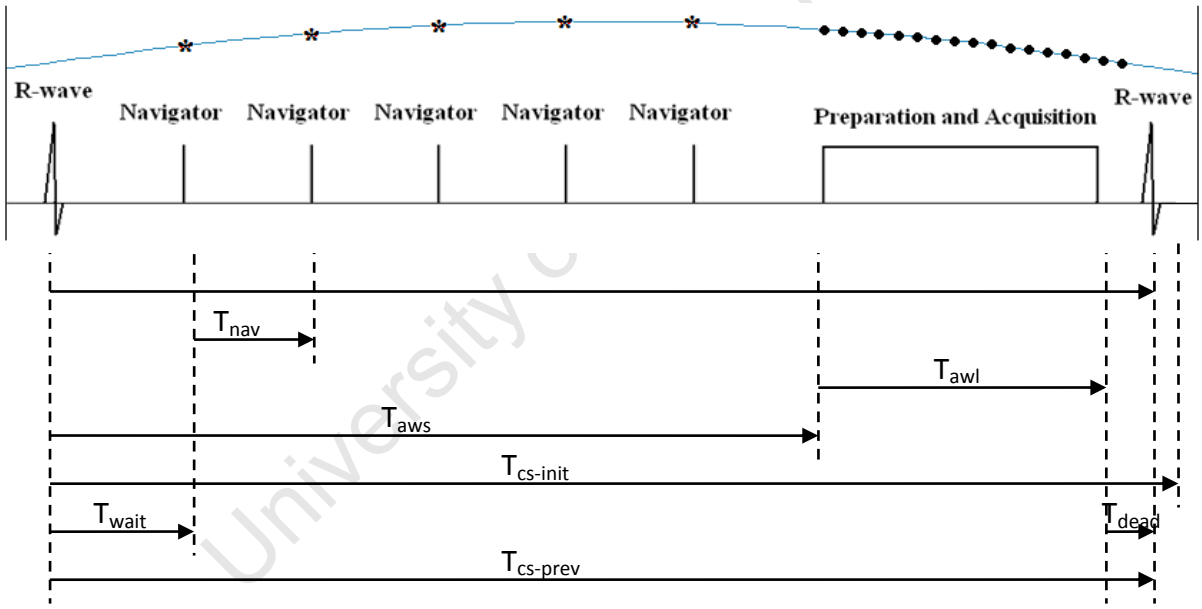

Figure 2.4: Schematic diagram of the timings for one cardiac cycle. The '*' represents samples obtained from the navigator, and the points represent values predicted by the model.

To increase the update rate of the control system's output during image acquisition, the signal is up sampled to equal the echo time of the sequence. The sample rate of the control system is 100 ms, the acquisition window in healthy people is approximately 200 ms, and the echo spacing of a gradient echo sequence is around 5 ms.

2.2.3 Simulation

The control system was tested by simulating the diaphragm measurement with a sine wave. Five navigator samples were acquired, followed by a further 5 samples with the error set equal to zero. This corresponds to a cardiac cycle where 5 navigator measurements are performed followed by an imaging segment of the same duration, which would be a very extreme case where the imaging segment lasts half of the cardiac cycle. In reality the imaging segment is typically around 200 ms in duration and rarely comprises even a quarter of the cardiac cycle.

In order to confirm that the control system would be able to update the model in real time to correct for both intra and inter subject changes in breathing and deviations from the model, we performed a simulation using the real breathing patterns of eight subjects. Navigator images were acquired to determine diaphragm position every 200 ms for a total duration of 3 minutes while the subjects breathed freely. The model was constructed using this data. The data were interpolated using Lagrangian interpolation to increase the number of samples to one every 100 ms. For the simulation, five navigator samples were supplied to the model as input, followed by 4 samples with the control system feedback error set equal to zero. This is equivalent to a cardiac cycle of 1000ms where 5 navigators are acquired every 100 ms, followed by an imaging segment of 400 ms, and 100 ms delay before the subsequent trigger. For each subject we computed the RMS error in order to assess the difference between the diaphragm positions predicted by the control system and the actual navigator readings.

2.2.4 Phantom Studies

To further test and validate the technique, a moving phantom experiment was performed. Scanning was performed on an Avanto 1.5 T (Siemens, Erlangen, Germany) whole body MRI scanner with a 2-element cardiac phased array coil. Data acquisition was performed with a two-dimensional navigator-gated bSSFP sequence, modified to incorporate real time motion correction as described above, with flip angle 70°; field of view 300 x 300 mm^2; matrix 512 x 512; 5 slices; slice thickness 2 mm.

A water phantom with a Perspex casing, 28 cm x 12 cm x 5 cm, was placed on a cart and moved manually in and out of the scanner to simulate tidal breathing, the amplitude of the motion being between 10 mm and 30 mm and the frequency being ±0.22 Hz. The duration of

the simulated cardiac cycle was set to 1000 ms using Siemens software simulator. The acquisition segment was from 600 to 900 ms after the ECG-trigger. Two acquisitions were performed using the standard navigator-gated bSSFP sequence with no motion correction and no respiratory gating, one with no motion and one while moving the phantom. Another acquisition was performed during which the phantom was again moved but the adapted navigated-bSSFP sequence with motion correction/prediction (i.e. with the control system implemented) was used. During the acquisitions with motion the phantom was moved with amplitude 25-30 mm.

In order to explore the performance of our method compared to gating for different amplitudes of motion, we then repeated two acquisitions for three different types of motion: small (amplitude ~10mm), medium (~20mm), and large (~30mm). For each type of motion, the phantom was first imaged using the adapted navigated-bSSFP sequence with motion correction (i.e. with the control system implemented), and then using the standard navigated-bSSFP sequence with gating with an acceptance window of 5mm.

In order to compare the quality of the phantom images for the different acquisitions, we compared the sharpness of the edges in the images. We considered a column of pixels through the image in the direction of the motion and measured the distance over which the voxel signal intensity along the column increases from 20 to 80% of its maximum value (rise distance) for each edge. Small distances indicate sharp edges, while blurring will lead to larger distances. This measurement was repeated for columns across the entire image and on all slices. From this data the mean rise distance for each edge was calculated for each acquisition and compared for the different acquisitions using a Student's t-test.

2.2.5 In Vivo Validation

In vivo scanning was performed on one subject on a 1.5 T Avanto (Siemens, Erlangen, Germany) MRI scanner with a 2-element cardiac phased array coil. The scan was acquired according to protocols that had been approved by the institutional review board of Imperial College London and the Faculty of Health Sciences Human Research Ethics Committee of the University of Cape Town. The subject provided written informed consent. Data acquisition was performed with a two-dimensional navigator-gated bSSFP sequence, modified to incorporate the motion correction control system; flip angle 70°; field of view 300 x 300 mm; matrix 256 x 256; and slice thickness 7 mm. The subject was asked to breathe

normally for all the acquisitions. The acquisition window within the cardiac cycle was set to 200 ms.

Three acquisitions were performed in the long axis view. The first acquisition was performed with no correction and no respiratory gating applied. For the second acquisition a gating window of 5 mm was placed at end-expiration. For the third acquisition the control system was applied with no gating window and a correction factor of 0.6 to correct between diaphragm displacement and cardiac displacement as has been suggested by Wang et al.(1995b).

2.3 Results

We present results for the simulations, phantom and in vivo studies to demonstrate how the control system compares to current methods of respiratory motion correction.

2.3.1 Simulation

Figure 2.5 shows how the output of the control system (right) follows the input (left) perfectly even though no input was acquired for 50% of the time, validating the approach taken.

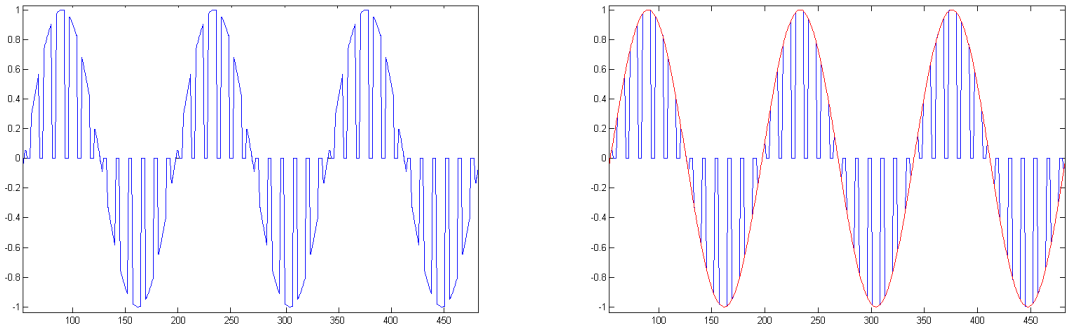

Figure 2.5: Input (Left) and Output (Right) of the control system when simulating the diaphragm motion with a sine wave; Blue: Navigator signal, Red: Control system output.

Using the physiological breathing patterns of eight subjects we confirm that the control system will adjust the model in real time to correct for deviations from a sinewave and for variations in breathing both within and between subjects. In Table 2.1, we present for each

subject the RMS error of the values predicted by the control system compared to the true diaphragm positions, as well as the range of the diaphragm motion. Figure 2.6 A shows the navigator values and the values predicted by the model for a random 16 s sample for one subject and figure 2.6 B shows the sample of a subject that demonstrated respiratory drift.

Table 2.1: Root mean squared (RMS) error and diaphragm range for the 8 volunteers that were scanned.

Subject	1	2	3	4	5	6	7	8	Mean
RMS error(mm)	0.66	0.94	0.66	0.55	0.62	0.82	0.71	0.49	0.68±0.14
Diaphragm range(mm)	14.25	15.58	11.80	15.21	16.16	17.27	13.38	12.53	14.52

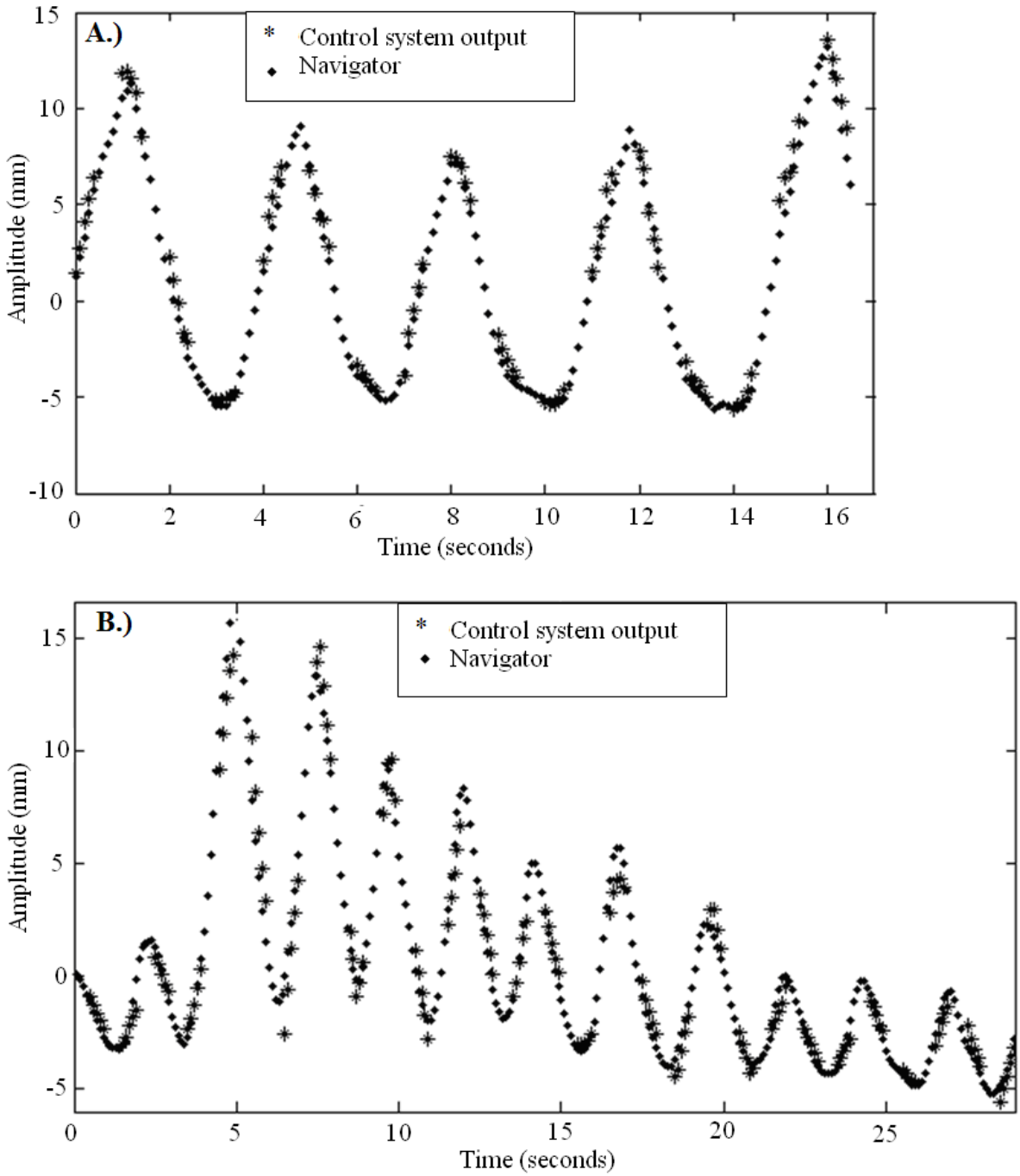

Figure 2.6: Comparison of diaphragm positions as measured using the navigator with diaphragm positions predicted using the control system for A) a subject with tidal breathing and B)a subject demonstrating respiratory drift. Points represent the navigator data and *'s the control system output.

2.3.2 Phantom Studies

Figure 2.7 shows example images for each of the different acquisitions and demonstrates how the voxel signal intensities were measured along a column in order to compute the sharpness of the edges. Increased blurring of the edges is clearly evident in figures 2.7c and e, which

were acquired with no motion correction and using the ARA with a 5 mm acceptance window, respectively. Figure 2.8 shows a comparison for the different acquisitions of plots of the voxel signal intensity as a function of position along the columns shown in red in the images in figure 2.7. For each acquisition, as a measure of edge sharpness, we compute the rise distance for each edge (labelled i-iv in figures 2.7 and 2.8) averaged over all columns in the image and all slices. Figures 2.9 and 2.10 show the differences between the rise distance of edge (i) for the different acquisitions.

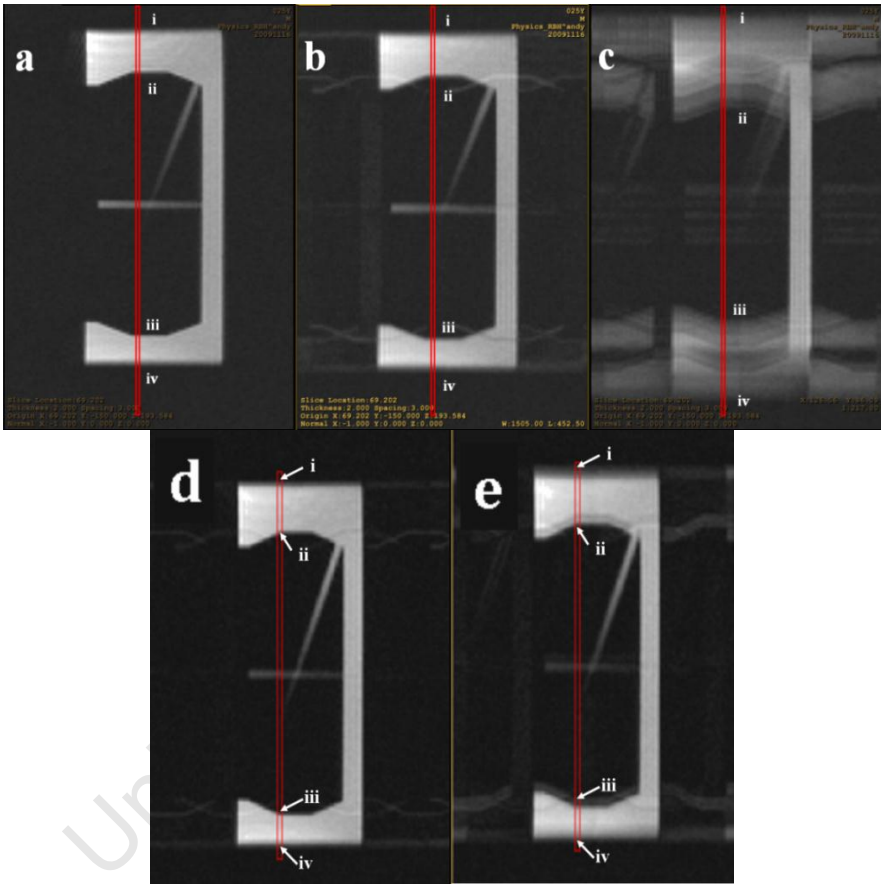

Figure 2.7: Images obtained during phantom scanning: a) no motion, no correction, no respiratory gating, b) motion & control system, c) motion, no correction, no respiratory gating, d) 30 mm motion & control system e) 30 mm motion & gating with 5 mm window. The red line illustrates a column in the direction of motion along which the image intensity is measured to evaluate the sharpness of the edges i to iv. During b) and c) the phantom was moved with amplitude 25-30 mm.

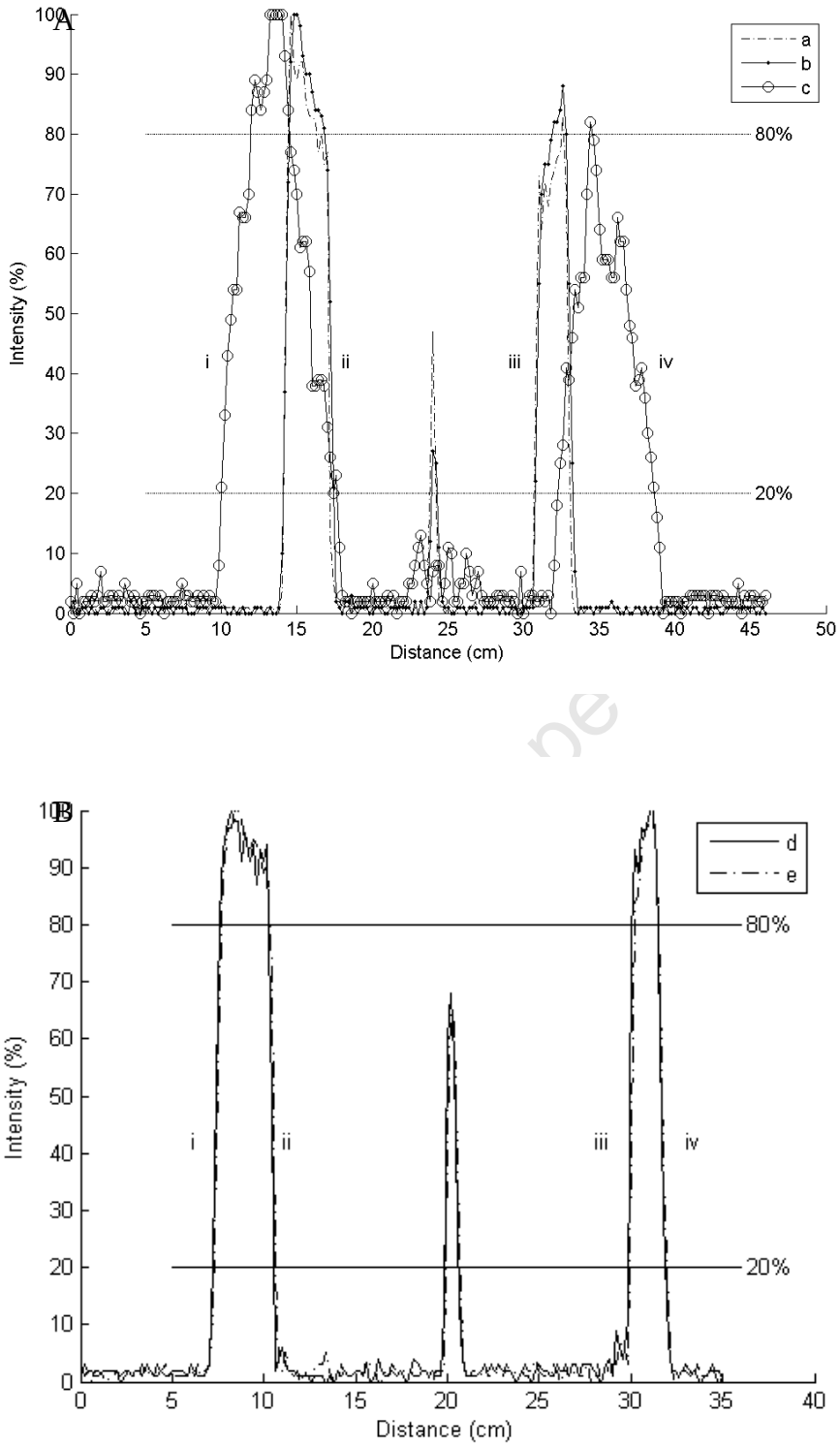

Figure 2.8: Plots of voxel signal intensity as a function of position along the column shown in red in the images in figure 2.7 in order to illustrate how the edge sharpness was measured. (A) presents a comparison of phantom scans with a) no motion, b) motion & control system, c) motion & no correction, while (B) presents a comparison of acquisitions with 30 mm motion acquired with d) the control system, and e) gating with a 5 mm acceptance window. During b) and c) the phantom was moved with amplitude 25-30 mm.

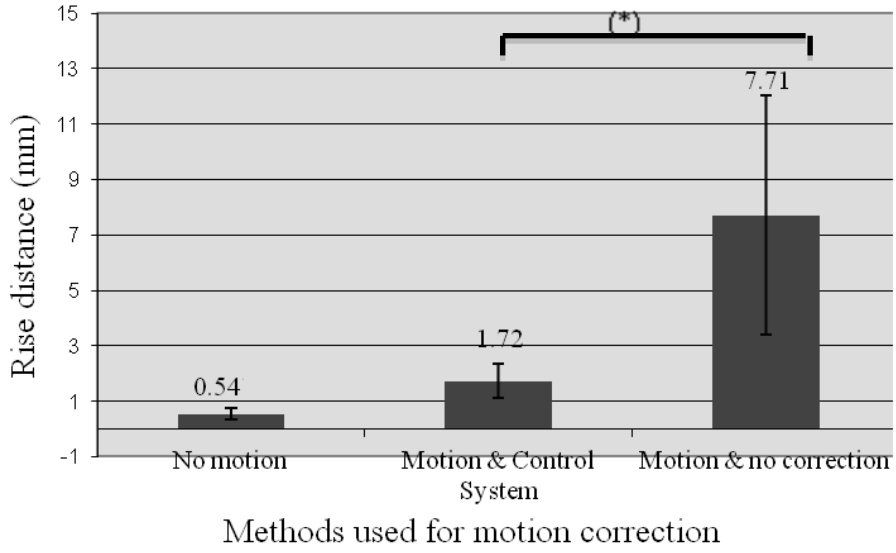

Figure 2.9: Comparison between the rise distances of edge (i) for the different acquisitions. The phantom was moved with amplitude of 25-30 mm.

*p< 0.001, Student's t-test

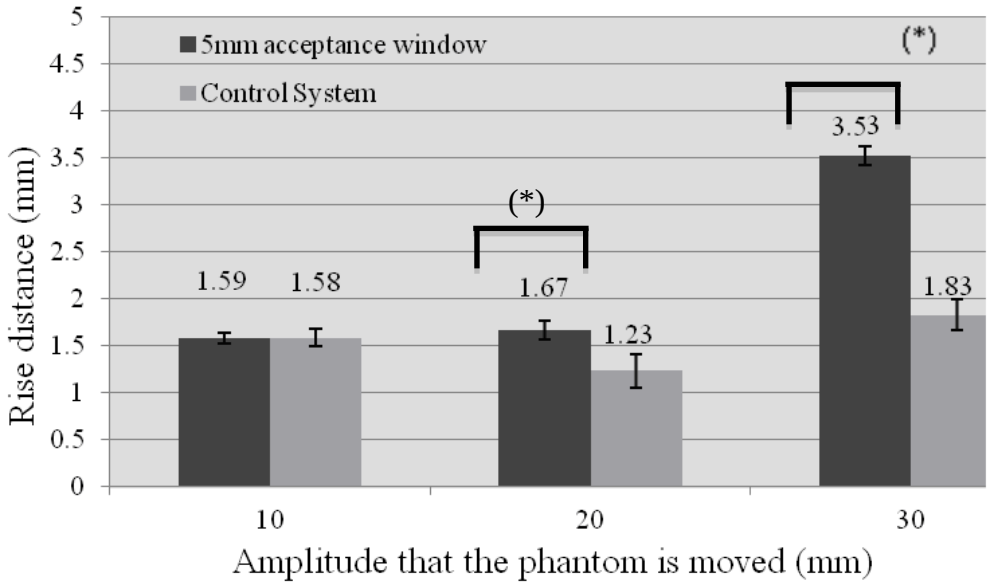

Figure 2.10: Comparison of the rise distances of edge (i) between the control system and navigator gating with a 5 mm acceptance window for different amplitudes of motion.

*p<0.001, Student's t-test.

In the presence of motion, the rise distance increases significantly ($p< 0.001$) if no motion correction and no respiratory gating is applied (Figure 2.9). For amplitude 10 mm, there is no significant difference between the sharpness of the edges using either the control system or the ARA with a 5 mm acceptance window. For motion greater than 20 mm, the edges are significantly sharper ($p< 0.001$) using the control system. The respiratory efficiencies for the navigator gated scans were 52%, 44% and 38% for 10mm, 20mm and 30mm amplitude, respectively, while the control system provides 100% respiratory efficiency.

2.3.3 In Vivo Validation

Images for the three in vivo acquisitions are shown in figure 2.11. The first acquisition (a) was performed with no correction and no respiratory gating applied; the second (b) with a gating window of 5 mm at end-expiration; and the third (c) using the control system with no gating window and a correction factor of 0.6 to correct between diaphragm displacement and cardiac displacement. For the three acquisitions, the maximum diaphragm displacements were 11, 12, and 12 mm, respectively, indicating that the respiratory motion was comparable. The respiratory efficiencies were 100%, 43% and 100%, respectively. There is significantly more blurring in (a), while images of acquisitions (b) and (c) are similar.

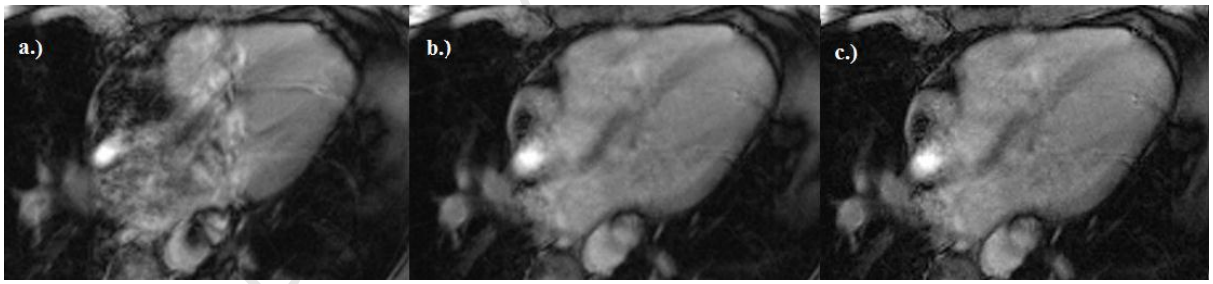

Figure 2.11: Images acquired in the long-axis view with a balanced SSFP sequence: a) no correction, b) navigator gating with a 5 mm acceptance window and c) motion correction using the control system.

2.4 Discussion

A prospective motion correction technique for cardiac- and respiratory-resolved MRI has been described and verified through simulation and phantom acquisitions and demonstrated in vivo.

The simulation with the sine wave input demonstrates that the control system locks to a frequency that has been determined by a short (~25 seconds) observation period and follows it perfectly if the input frequency and amplitude remains the same. Using the respiratory traces of 8 subjects, we demonstrate how the control system is updated in real time and adjusts to variations in the frequency and amplitude of the input signal. In figure 2.6 it can be seen that the variation in frequency caused by the pause at end-expiration is dealt with adequately. The control system deals with respiratory drift satisfactorily, as demonstrated in figure 2.6B. The average RMS error of 0.68 mm is significantly smaller than the 5 mm width of the acceptance window used in gating.

The phantom results confirm that the slice position is updated by the control system in real time, resulting in successful slice following and images with minimal blurring. For amplitudes of motion greater than 20 mm, the control system performed significantly better than gating with an acceptance window of 5 mm. Despite the same 5mm acceptance window, a larger range of motion revealed less sharp edges during the gated image acquisition as the position of the phantom changed more rapidly and covered more distance during the acquisition of individual k-space lines. Especially in subjects with exaggerated breathing, the improvements in respiratory efficiency and image quality will be significant.

While the in vivo images from the gated sequence and the control system are of similar quality (figure 2.11b, c), the images using the control system were acquired with a 100% respiratory efficiency, halving the scan time. Comparison to images (figure 2.11a) acquired without any correction or gating confirms the need for motion correction and the presence of significant respiratory motion (±12 mm diaphragm displacement) during the acquisition.

Since the correction factor of 0.6 is an estimate derived from previous studies this is not necessarily the correct ratio for each subject (Wang et al., 1995b). The correction factor only takes into account the inferior-superior motion of the heart and does not account for the rest of the non-rigid transformation parameters. The control system can be combined with subject specific motion models to further improve motion correction. The present method, which provides in real time the position of the diaphragm throughout the imaging segment, offers a significant improvement over standard slice following where the navigator position prior to the imaging segment is used and becomes increasingly outdated.

The control system is being incorporated in a biofeedback system developed by Jhooti et al (Jhooti et al., 2011). The visual feedback system guides the subject's breathing by

implementing multiple navigators between the R-wave and the imaging segment. During the navigator dead-time throughout the imaging segment, no positional information is available to the feedback system. This results in a lag of ~400 ms which produces a jerky motion in the feedback. The control system can be incorporated in the feedback loop, producing a smoother and easier to follow feedback to subjects.

2.5 Conclusion

A new approach to respiratory motion correction for cardiac imaging has been developed and validated. By accurately predicting the position of the diaphragm throughout the imaging segment during any cardiac sequence that is not acquired as a CINE sequence including, coronary MRA, black blood imaging, and delayed enhancement imaging, the gating window can be increased or even omitted.

2.6 Acknowledgements

This project was funded by the SA/Norway Research Cooperation Programme. The South African Research Chairs Initiative of the Department of Science and Technology and National Research Foundation of South Africa, Medical Research Council of South Africa. This project was supported by the NIHR Cardiovascular Biomedical Research Unit of Royal Brompton and Harefield NHS Foundation Trust and Imperial College London.

3. Chapter 3

Subject specific model

3.1 Abstract

Respiratory motion is a major problem in cardiac MRI. In this work the displacement of the heart relative to the diaphragm was investigated. A subject specific non-linear elliptical affine model has been developed in order to incorporate the effect of hysteresis in motion correction. Nine healthy volunteers participated in a study in which the diaphragm position and an image of the heart were acquired during each cardiac cycle whilst breathing freely. The elliptical model was compared to a linear affine model and the results show that the elliptical model performed significantly ($p < 0.05$) better than the linear model. Further it has been established that the model can be constructed within ~25s, which makes it feasible to perform a short pre-scan to construct the model, so that subject specific prospective motion correction of the heart can be integrated into structural cardiac MRI sequences.

Key words: Cardiac magnetic resonance imaging, respiratory motion correction, elliptical affine model, subject specific, hysteresis

3.2 Introduction

Limiting the effects of motion in MRI (Magnetic Resonance Imaging) remains a challenge, especially in cardiac MRI. Both cardiac motion due to the beating of the heart and respiratory motion need to be considered. The former is successfully managed with cardiac gating. The latter is more of a problem and many techniques have been suggested, of which only the most significant are summarized here.

Breath hold techniques are limited to scans that can be completed in 20-30 s or have to be done in multiple breath holds. Since the exact same breath hold position is rarely achieved and drift during breath hold also occurs, motion artefacts will be present (Holland et al., 1998, Jahnke et al., 2006). Furthermore, patients often struggle to hold their breath even for short periods of time.

Various free breathing techniques have been developed to manage motion in cardiac MRI. Most rely on navigators to monitor the inferior-superior motion of the right hemi-diaphragm during MR data acquisition to obtain a real time update of respiratory motion and use this to either perform respiratory gating, or to prospectively or retrospectively correct for the motion (Li et al., 1996, Nehrke et al., 2001). Respiratory gating accepts or rejects measurement data depending on the current diaphragm position. A 2.5-5 mm acceptance window at end-expiration is typically used to achieve high resolution images, but reduces the scan efficiency by roughly 30-50% (Stuber et al., 1999, Serfaty et al., 2000, Manke et al., 2002b, Zhang et al., 2006). Including phase-ordering and section tracking reduces the scan time without reducing the image quality (Nehrke et al., 2001).

Prospective correction techniques enable further widening of the acceptance window (Danias et al., 1997, Burger et al., 2010). A correction factor is required to account for the difference in motion of the heart and the diaphragm. According to Nehrke et al. the dominant motion of the heart is in the inferior-superior direction with significantly less motion in the left-right and anterior-posterior directions (Nehrke et al., 2001). For this reason it is common practice to neglect the smaller components and correct only for the inferior-superior motion (Wang et al., 1995b). Studies have shown that cardiac displacements range from 0.22 (range 0.14 to 0.31) to 0.57 (standard deviation 0.26) of the diaphragm displacement (Wang et al., 1995b,

Serfaty et al., 2000). A correction factor of 0.6 has been suggested for coronary imaging (Botnar et al., 1999, Stuber et al., 2001).

Previous studies have shown that there is significant inter-subject variability in the transformation and rotation of the heart from end-expiration to end-inspiration (McLeish et al., 2002, Shechter et al., 2004). Schechter et al. also noted that the diaphragm's range of motion is much smaller during free breathing with an average displacement of 15 mm (range: 10 – 19 mm) (Bogren et al., 1977), compared to displacements as large as 40 mm during breath hold (McLeish et al., 2002). Subject specific correction factors, or better yet, a model of a subject's breathing pattern, could greatly improve prospective motion correction.

Breath hold studies have aimed to model the relationship between diaphragm and cardiac motion (Manke et al., 2002a). The application of the results is limited, however, by the fact that the relationship between the heart and diaphragm is significantly different during breath hold and free breathing (Serfaty et al., 2000). Another approach has applied multiple navigators through the heart in real time to construct a model (Nehrke and Börnert, 2005). Here, however, only a few points on the heart were actually imaged. Manke et al. performed a study using low resolution 3D images to construct an affine transformation model for subject specific motion (Manke et al., 2002b). Although the results show good following of the heart, it does not address the hysteretic effect, since the model is linear and does not distinguish between inspiration and expiration. Nehrke et al. tracked the right hemi-diaphragm and left ventricular wall of the heart by placing a navigator over each during free breathing. The results demonstrate the presence of hysteresis in the respiratory pattern. Inspiration and expiration follow different paths and the direction is always counter clockwise, from an anterior view. The authors also found significant inter-subject variation (Nehrke et al., 2001).

We know that during expiration the diaphragm pushes up against the heart causing an upward translation, cranio-dorsal rotation and compression of the heart (Shechter et al., 2004). If, however, it was possible to know exactly what transformation the heart undergoes relative to the diaphragm due to respiration for each subject being scanned prior to the image acquisition, a much more accurate following could be accomplished, improving image quality and reducing artifacts. Ideally, the hysteresis should also be compensated for by adjusting the correction factor for any respiratory state also differentiating between inspiration and expiration.

In this study, we construct a complete model of heart position relative to diaphragm position by repeatedly imaging the heart, together with the diaphragm position, in free breathing during different times of the respiratory cycle, providing detailed information of respiration-induced cardiac motion. We demonstrate that a subject specific model can be created using a short pre-scan (~25 seconds), which can be used to prospectively correct for respiratory motion in free breathing cardiac MRI thus improving image quality and reducing scan time.

3.3 Methods

Nine healthy volunteers (five male) with no history of cardiovascular disease or other known risk factors, took part in this study. The mean (±standard deviation) heart and breathing rate of the volunteers were 67 ± 9 bpm (beats per minute) and 21 ± 15 breaths per minute. The subjects were between the ages of 26 and 50 with an average (± standard deviation) age of 35.8 ± 9.6 years. All scans were acquired according to protocols that had been approved by the institutional reviews board of Imperial College London and the Faculty of Health Sciences Human Research Ethics Committee of the University of Cape Town. Scans were acquired on a Magnetom Avanto 1.5 T (Siemens, Erlangen, Germany) scanner at the Royal Brompton Hospital, London. All subjects provided written informed consent. A single-shot image and a navigator reading were acquired during each cardiac cycle. Data acquisition was performed with a two-dimensional balanced Steady-State Free Precession (bSSFP) sequence with navigators. A navigator preceded each single-shot acquisition. Figure 3.1 illustrates the timing of the sequence within the cardiac cycle. A CINE image series was acquired prior to the bSSFP acquisition in order to determine the best trigger delay time for each subject.

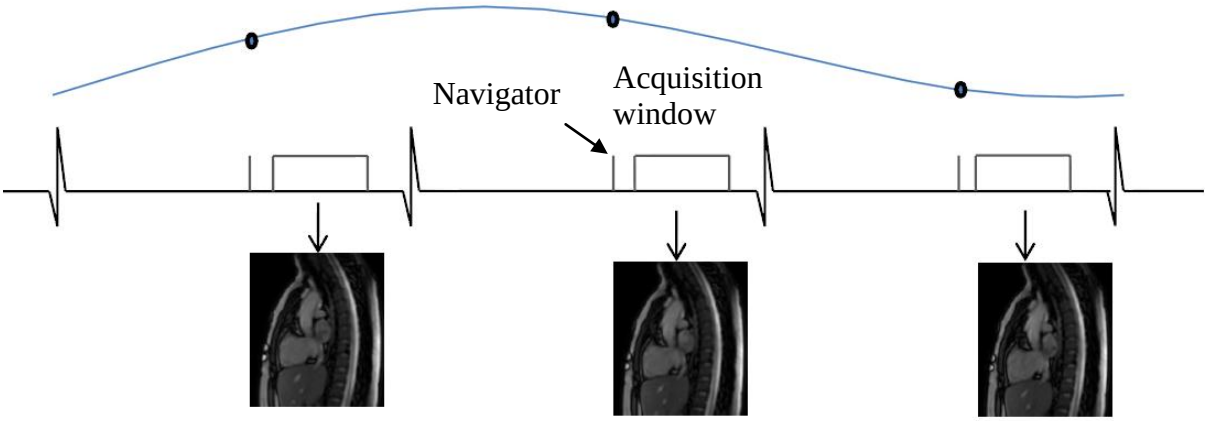

Figure 3.1: Schematic diagram of the timing of the sequence within the cardiac cycle. The respiratory motion of the diaphragm is represented by the curve above the ECG trace and the dots superimposed on this curve represent the navigator readings. The single-shot acquisition is performed near the end of the cardiac cycle to reduce cardiac motion. Each single-shot acquisition is preceded by a navigator.

The navigator was positioned through the dome of the right hemi-diaphragm and was interleaved to record the diaphragm position prior to the acquisition window during each cardiac cycle. Acquisitions were performed in the sagittal and coronal orientations. In each acquisition, a single slice was imaged repeatedly for 90 cardiac cycles while subjects breathed freely. As such, we obtain images of a single sagittal and coronal slice at 90 different time points in the respiratory cycle, together with the corresponding position of the right hemi-diaphragm for each image. Time to complete an acquisition was about 90 seconds, depending on the subject's heart rate. Each acquisition was repeated twice, with the sagittal and coronal acquisitions interleaved, resulting in an interval of roughly 90 s (depending on the heart rate) between acquisitions of the same orientation. Sequence parameters were: flip angle 70°; acquisition window length (time to complete single-shot bSSFP image) 320.1 ms; TR 2.8 ms; TE 1.8 ms; bandwidth 560 Hz/px; slice thickness 8 mm; FOV (Field of View) 360 x 360 mm; percentage sampling 96%; matrix size 112 x 96, interpolated to 224 x 192; reconstructed in-plane resolution 1.61 mm x 1.88 mm, and navigator resolution 1 mm. Image data were acquired as late as possible in the cardiac cycle to minimize the effect of cardiac motion, with a typical gating delay of 600-650 ms. The precise placement of the acquisition window for each subject was determined by examining a CINE image. Subjects were asked to breathe normally.

After completion of the scans the images were cropped and segmented with a fully automated algorithm to remove regions that are not of interest, such as the chest wall and spinal cord, but included the whole heart and great vessels below the aortic arch. The different steps of the algorithm are illustrated in figure 3.2. The algorithm calculates the gradient of signal intensity between adjacent pixel pairs along eight evenly spaced spokes from the centre of the image, as demonstrated in figure 3.2(b). The maximum gradient indicates the edge of the heart in the image. The image is thresholded using the mean of the signal intensities of the two pixels with the maximum gradient. All the pixels with signal intensity below the threshold are set to zero and those with signal intensity above the threshold are set to one (figure 3.2(c)). All the connected pixels are grouped together and the size of each cluster is calculated (figure 3.2(d)). The biggest cluster is assumed to be the heart. The assumption proved to be valid since it was correct for all images of all the acquisitions. The original signal intensities of the biggest cluster are reassigned and the remaining clusters are set to zero (figure 3.2(e)).

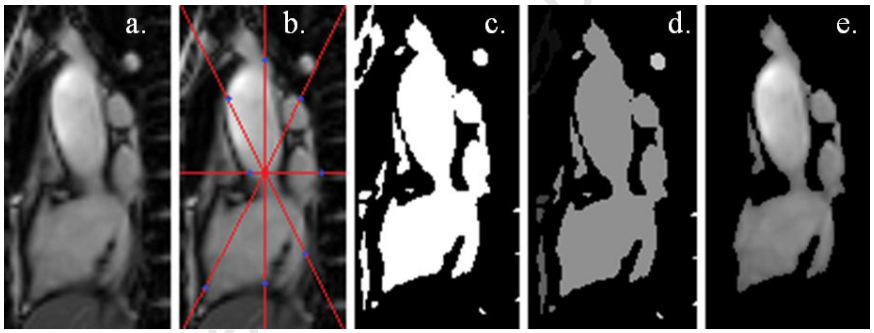

Figure 3.2: Automated segmentation process. (a) Cropped image; (b) Spokes along which the gradient between adjacent pixel pairs is calculated are indicated in red. The sharpest edges are represented by the blue points. (c) Image after thresholding; (d) Result of clustering; (e) The smaller clusters are set to zero and signal intensities of the largest cluster are reassigned.

All the segmented images were then co-registered to the first image of the corresponding acquisition using an edge sensitive non-rigid/affine registration algorithm that was implemented in MATLAB (Klein et al., 2011). Matrices describing the transformation of individual images to their first image are denoted by **T**, while **M** denotes the transformation computed using the model in combination with navigator readings. For the remainder of the text the transformation matrices obtained from co-registration of individual images from the first acquisition to their first image will be referred to as matrix $\boldsymbol{T}^{1}$, and the transformation

matrices from co-registration of images from the second acquisition as $\boldsymbol{T^2}$ as shown in equation 3.1:

$$T^m(k) = \begin{bmatrix} T_{11} & T_{12} & T_{13} \\ T_{21} & T_{22} & T_{23} \\ \mathbf{0} & \mathbf{0} & \mathbf{1} \end{bmatrix} \begin{matrix} m = 1 \; for \; first \; acquisition \\ m = 2 \; for \; second \; acquisition \end{matrix} \tag{3.1}$$

$$1 \leq k \leq Total \; number \; of \; cardiac \; cycles \tag{3.2}$$

The superior/inferior direction was taken as the y-axis for the sagittal and the coronal images, with superior being positive. The x-axis in the coronal images was from left to right, with right being positive. The x-axis in the sagittal images was along the anterior/posterior direction, with anterior being positive. The diaphragm displacements (*nav*(k)) throughout each acquisition were calculated relative to the first diaphragm position for that acquisition (equation 3.3), and paired with the transformation matrix of the same cardiac cycle.

For each acquisition

$$nav(k) = navigatorvalue(k) - navigatorvalue(1) \qquad 1 \leq k \leq 90. \tag{3.3}$$

For each element in the transformation matrix $\boldsymbol{T^1}$, the value at each time point was plotted as a function of the navigator displacement for the corresponding cardiac cycle. This was done for both the first sagittal and coronal acquisitions. This enabled us to assess the relationship between diaphragm displacement and each component of the transformation matrix. For each component, the data was fitted to an ellipse superimposed on a straight line. This was done for each subject, thus yielding a subject specific relationship between the displacement of the diaphragm and the heart that takes hysteresis into account. For any navigator measurement, each component of the model transformation matrix $\boldsymbol{M}$ can therefore be calculated, and the position of the heart determined. The model is given by,

$$\boldsymbol{M} = \begin{bmatrix} M_{11} & M_{12} & M_{13} \\ M_{21} & M_{22} & M_{23} \\ \mathbf{0} & \mathbf{0} & \mathbf{1} \end{bmatrix}, \tag{3.4}$$

where for each cardiac cycle k,

$$M_{ij}(k) = \left(\pm \left(\frac{b_{ij}}{a_{ij}} \times \sqrt{a_{ij}^2 - \left(nav(k) - d_{ij}\right)^2} \right) + m_{ij} \times nav(k) + c_{ij} \right) \times sf, \begin{matrix} 1 \leq i \leq 2 \\ 1 \leq j \leq 3 \end{matrix} \quad (3.5)$$

$$sf = \frac{FoV}{Matrix\ size} \quad (3.6)$$

M is the transformation matrix of the model, m_{ij} is the gradient of the straight line, a_{ij} is the length of the long axis of the ellipse, b_{ij} is the length of the short axis of the ellipse, c_{ij} is the y-intercept, d_{ij} is the x-offset, and *sf* scales the values to millimetres. Figure 3.3 shows the typical shape of the model.

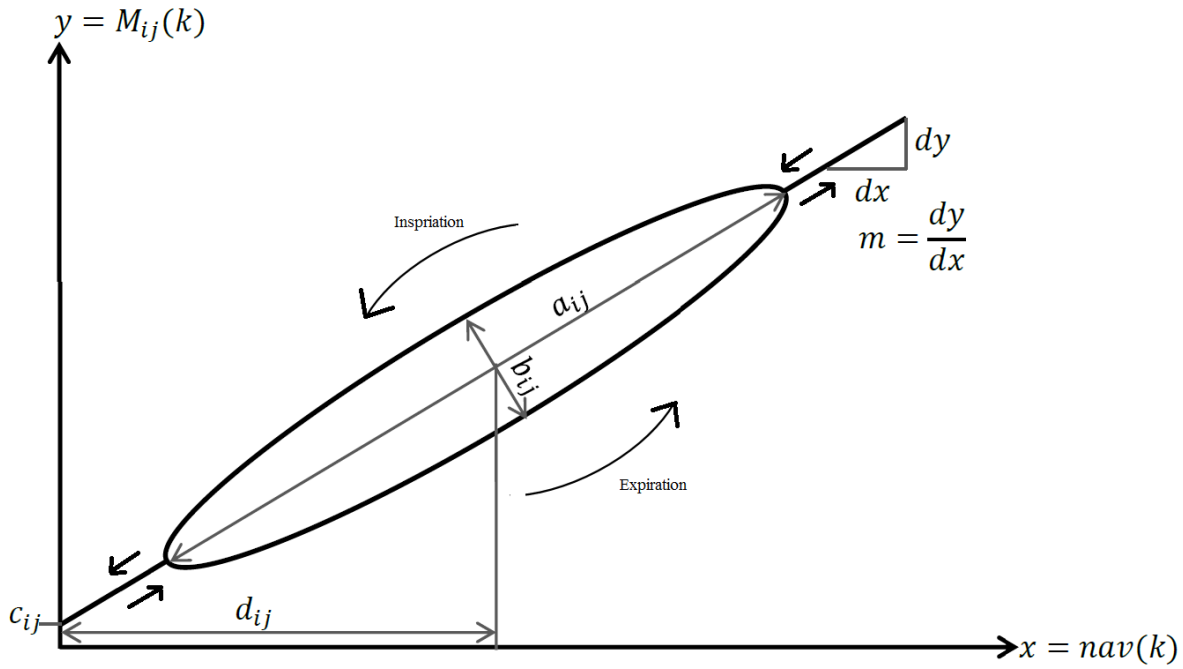

Figure 3.3: The model used to represent displacement of the heart due to respiratory motion. Each component of the model matrix consists of such a model. In the figure m_{ij} is the gradient of the straight line, a_{ij} is the length of the long axis of the ellipse, b_{ij} is the length of the short axis of the ellipse, c_{ij} is the y-intercept, d_{ij} is the x-offset.

The parameters a_{ij}, b_{ij}, c_{ij}, d_{ij} and m_{ij} of equation 3.5 were altered iteratively to minimize the error function given by equation 3.7 to ensure the best fit for the measured data for a given subject.

$$\sum_{k=1}^{n} e_{ij}(k) = \frac{\sqrt{\left(T^{1}{}_{ij}(k) - M_{ij}(k)\right)^{2}}}{n}, \tag{3.7}$$

in which $\boldsymbol{T^1}$ is the affine matrix calculated from the co-registration of the images of the first acquisition, $\boldsymbol{M}$ is the model affine matrix, and $\boldsymbol{e}$ is the error of the model.

The model was validated using the images from the second sagittal and coronal acquisitions. As before, the images from all 90 cardiac cycles of these acquisitions were co-registered to their first images using the non-rigid affine transformation implemented in MATLAB (Klein et al., 2011), yielding transformation matrices $T^2(k)$, for every cardiac cycle k. Using the navigator outputs for each cardiac cycle combined with the subject specific model M that was constructed from the first acquisition with the same orientation, yields the transformation matrix M(k) that would predict the most likely position of the heart for said diaphragm position. In order to compare the model prediction of the heart position with the position we actually measured, we considered the effects of the two transformations on a point with x- and y-coordinate 56 mm (ie. one quarter of the FOV) from the centre of the image. This point was chosen as it lies on the most superior edge of the heart and as such represents a worst case scenario. Each component of the transformation matrices predicted using the model for all 90 cardiac cycles was compared to each component of the corresponding transformation matrices obtained using co-registration at this point. The error was computed using equation 3.8, where T^2 is the affine transformation matrix from the second acquisition and M the model constructed from the first acquisition.

$$\sum_{k=1}^{n} e_{ij}(k) = \frac{\sqrt{\left(T^{2}{}_{ij}(k) - M_{ij}(k)\right)^{2}}}{n}, \tag{3.8}$$

The elliptical model was compared to a straight line model that does not account for hysteresis. The straight line model used was constructed in the same manner as the elliptical model, but without the ellipse added to the equation. This effectively represents a linear non-rigid model. The straight line model is defined by equations 3.9 and 3.10:

$$\boldsymbol{Msl} = \begin{bmatrix} Msl_{11} & Msl_{12} & Msl_{13} \\ Msl_{21} & Msl_{22} & Msl_{23} \\ \mathbf{0} & \mathbf{0} & \mathbf{1} \end{bmatrix} \tag{3.9}$$

$$Msl_{ij} = m_{ij} \times nav(k) + c_{ij} \tag{3.10}$$

The error of the straight line model was computed using equation 3.11, where $\boldsymbol{T^2}$ is the affine transformation matrix from the second acquisition and $\boldsymbol{M_{sl}}$ the straight line model constructed from the first acquisition.

$$\sum_{k=1}^{n} e_{ij}(k) = \frac{\sqrt{\left(T^2{}_{ij}(k) - Msl_{ij}(k)\right)^2}}{n}, \tag{3.11}$$

The elliptical model was first validated using all 90 measurements (i.e. 90 images and navigator readings acquired over 90 cardiac cycles) acquired in the first acquisition of each subject to construct the model for testing against the 90 measurements of the second acquisition. In order to investigate the minimum number of cardiac cycles required in a pre-scan to yield a model with acceptable accuracy, we reduced the number of measurements used to construct the model and then re-tested the model against the 90 measurements of the second acquisition. Since the primary purpose of using a model is to reduce the scan time whilst maintaining the image quality, it is important to know how long the pre-scan will have to be.

We repeated the process of creating the model with measurements from the first acquisition, ranging from five to 90 in increments of five. The RMS error of the model was again determined by investigating the prediction accuracy of the model constructed from these different numbers of measurements for all 90 measurements of the second acquisition. Each component of each transformation matrix predicted using the model ($\boldsymbol{M}$) was compared to each component of the corresponding transformation matrix ($\boldsymbol{T^2}$) obtained using co-registration of the images.

3.4 Results

In agreement with the literature, we observe significant variation between the subjects. The average diaphragm displacement was 18.8 (±7.35) mm peak to peak in the superior/inferior direction, ranging from 12 mm to 33 mm in the subjects with the smallest and largest displacements, respectively. Since hysteresis was present in all the subjects, although small in some of the subjects, the elliptical model performed better, producing a smaller RMS error, than the straight line model in all the subjects.

The regression plots for the sagittal images of one of the subjects are presented in figure 3.4. From the plot it is evident that the elliptical curve fits the points for M_{11}, M_{12}, M_{13}, M_{21} and M_{22} very well. Correlations between the model and actual values for each navigator reading for these components were 0.95, 0.87, 0.97, 0.95 and 0.88, respectively (Pearson's *r*). Using a straight line model the correlation coefficients for these components were 0.85, 0.68, 0.92, 0.85 and 0.7, respectively. For M_{22} the data points were more scattered with correlation coefficient 0.66, but the elliptical model still provides a better fit than a straight line (r = 0.15). In figure 3.5 we present difference maps in order to compare the results of affine co-registration (Klein et al., 2011), compared to elliptical and linear models applied to a sagittal image of a subject. The results of the elliptical model and co-registration are almost identical.

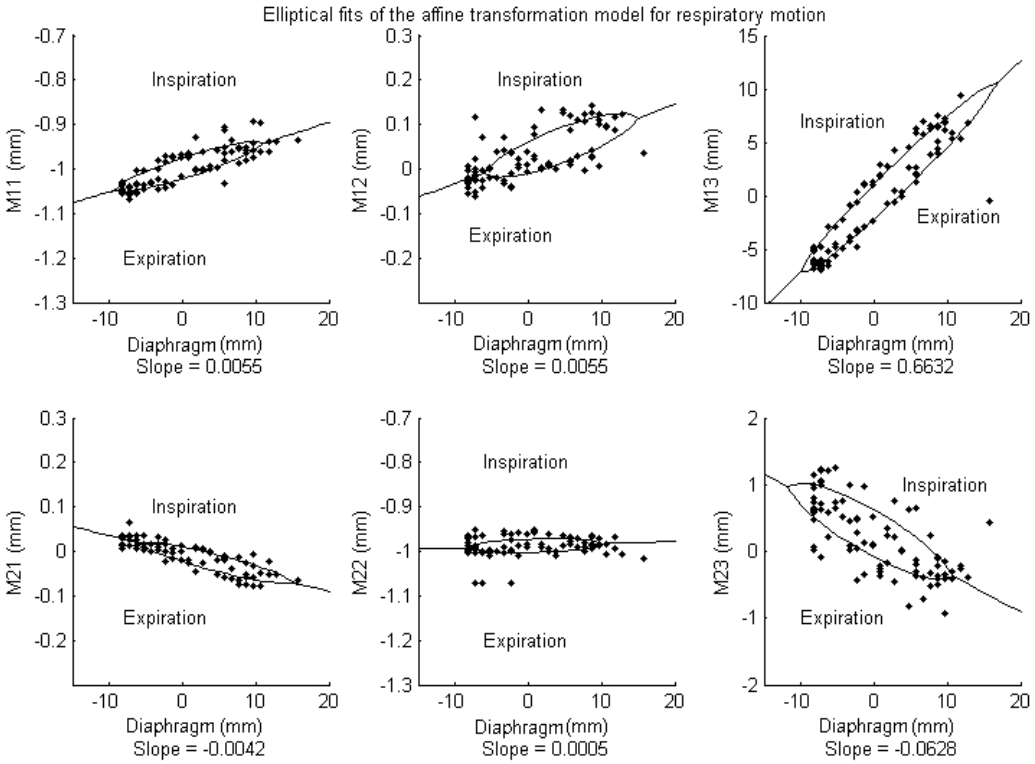

Figure 3.4: The components of the affine transformation matrix plotted against the corresponding navigator displacements for all measurements for one subject. Images were acquired during free breathing as late as possible in the cardiac cycle, preceded by the navigator. The curves fitted for each component are shown, with the gradient of the fit given below each plot.

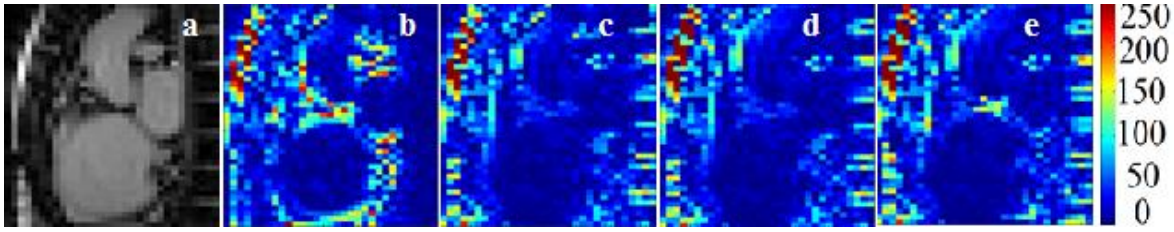

Figure 3.5: Shows the target sagittal image of a subject. The remaining images are all difference images between the target and b) an uncorrected image; c) an image transformed using affine registration (Klein et al., 2011); d) an image transformed using the elliptical model; and e) an image transformed using the linear model. The target and original images are from the second acquisition. The model was created using the first acquisition and applied to the images from the second acquisition.

Figures 3.6 to 3.8 show the mean and standard deviation of the gradient (figure 3.6), long axis (figure 3.7), and short axis (figure 3.8) for the different components of the model in the coronal and sagittal planes averaged over all the subjects. The close agreement between the values of M_{11}, M_{12} and M_{13} computed from data acquired in the sagittal and coronal planes confirms that the inferior-superior components of the model correlate well. The results indicate a clear trend in the values of the different components, but also the presence of inter-subject variation stressing the need for a subject specific model. Figure 3.9 illustrates the inter-subject variation in the respiratory motion models observed in this study.

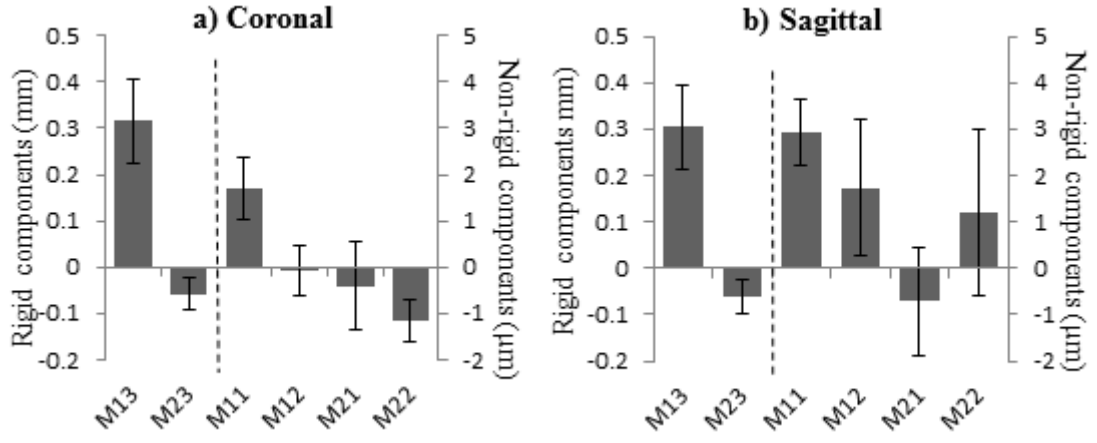

Figure 3.6.a) Coronal; and **b)** sagittal. Mean (± standard deviation indicated by error bars) of the gradient (m) for the different components of the model averaged over all subjects. The left axis is for the rigid components (M_{13} and M_{23}), the axis on the right is for the non-rigid components (M_{11}, M_{12}, M_{21} and M_{22}).

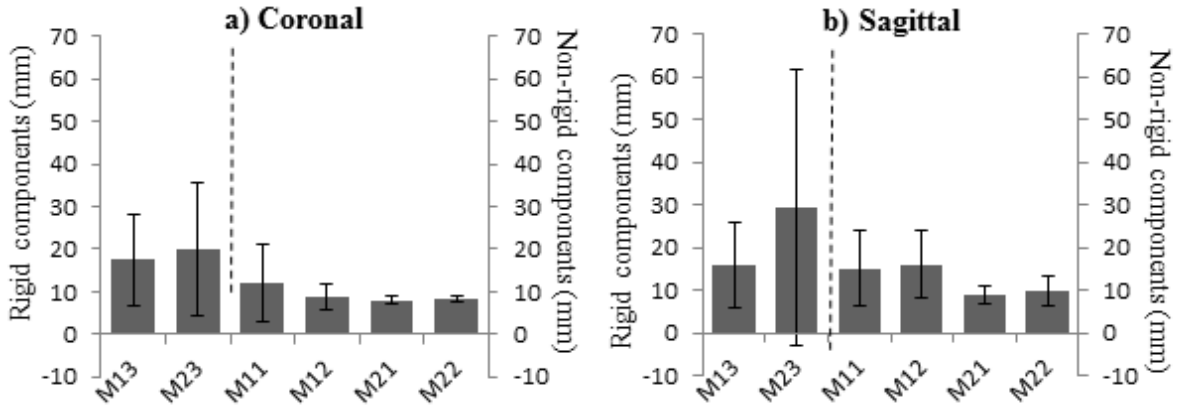

Figure 3.7.a) Coronal; and **b)** sagittal. Mean (± standard deviation indicated by error bars) of the long axis (*a*) for each component of the model averaged over all subjects. The left axis is for the rigid components (M_{13} and M_{23}), the axis on the right is for the non-rigid components (M_{11}, M_{12}, M_{21} and M_{22}).

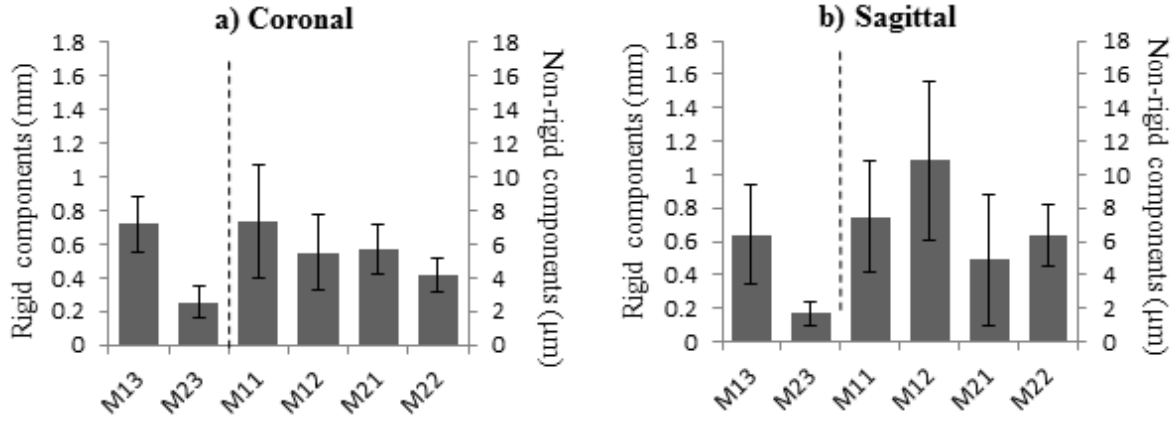

Figure 3.8.a) Coronal; and **b)** Sagittal. Mean (± standard deviation indicated by error bars) of the short axis (*b*) for each component of the model averaged over all subjects The left axis is for the rigid components (M_{13} and M_{23}), the axis on the right is for the non-rigid components (M_{11}, M_{12}, M_{21} and M_{22}).

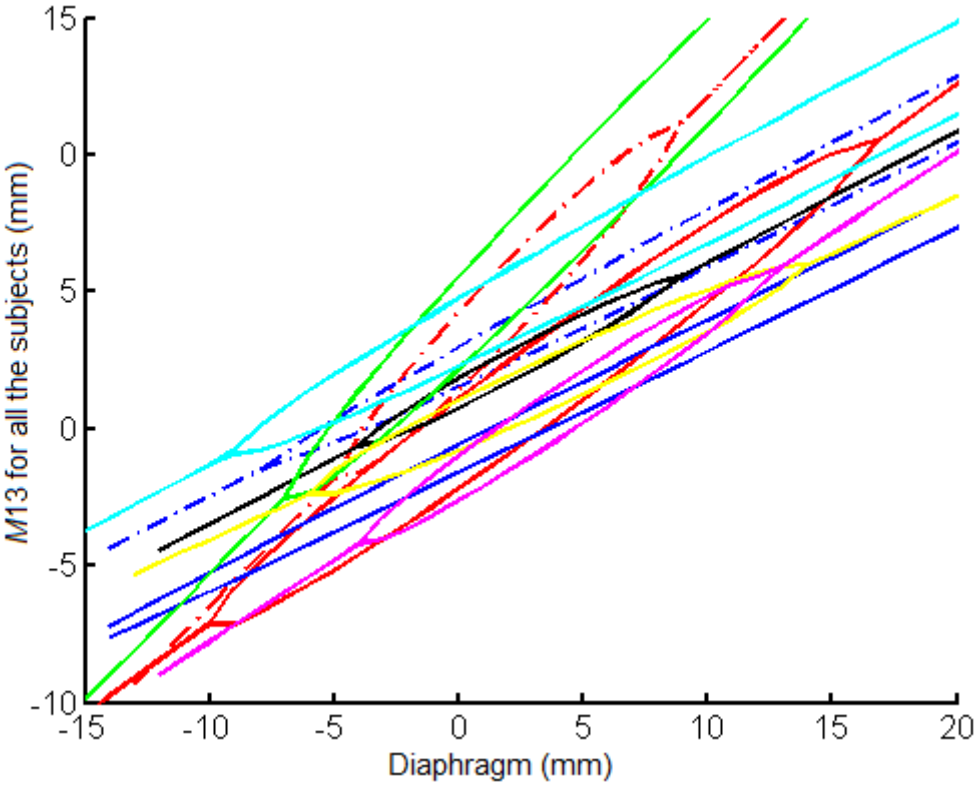

Figure 3.9: The superior-inferior translation (M_{13}) of the sagittal image for the different subjects shows the inter-subject variation in the gradients, the amount of hysteresis, and the depth of breathing.

In figure 3.10 we present the root-mean-square (RMS) error (error bars are ± standard deviation) for each component averaged over all subjects and all cardiac cycles when comparing the transformation matrices obtained from the co-registration to those obtained using the navigator outputs with either the elliptical or straight line models. The elliptical model demonstrates significantly smaller errors ($p < 0.05$, paired Student's t-test) for all the components as well as less variability than the straight line model.

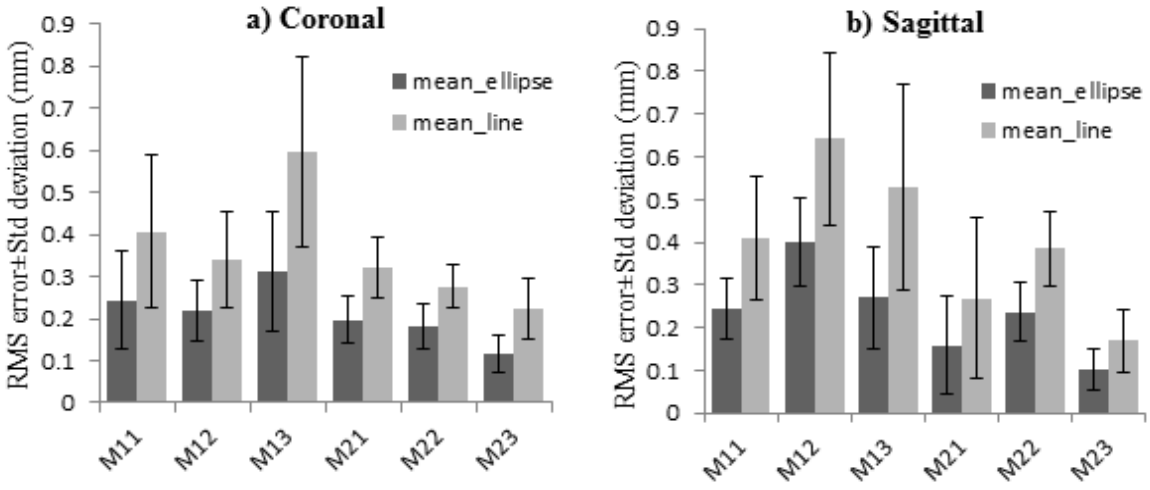

Figure 3.10: Mean RMS error of the model (***M***), constructed from the first acquisition, compared with the affine registration matrices from the second acquisition ($\boldsymbol{T}^2$) (± standard deviation indicated by error bars), averaged over all the volunteers and all cardiac cycles during free breathing with images acquired as late as possible in the cardiac cycle with the navigator preceding each image acquisition. Data on the left is based on coronal images and that on the right on sagittal. The results for the ellipse superimposed on a straight line non-rigid model as well as a linear non-rigid model are presented to demonstrate the improvement when using an elliptical model to address the hysteresis.

The errors in both orientations are below pixel size and are small enough for the model to be used in coronary imaging, at an imaging resolution of 1 mm (Wang et al., 1995b). Errors in the coronal plane are slightly smaller than in the sagittal plane. This is attributed to the image segmentation algorithm that performed better on the images acquired in the coronal plane. The images acquired in the sagittal plane do not have the clear edge between myocardium and adjacent anatomy, whereas in the coronal plane the myocardium is surrounded by lung tissue giving a sharp edge/contrast.

In order to determine how many cardiac cycles need to be imaged in a pre-scan to build a subject specific model with sufficient accuracy for prospective correction of motion, we investigated the effect of reducing the number of measurements used to construct the model.

The mean (± standard deviation) RMS error across all the subjects is displayed in figure 3.11. After 25 to 30 samples a plateau is reached so that little improvement is offered by a longer pre-scan. This is particularly evident in M11, M13 and M23 of the coronal and M11, M21, M22, M23 of the sagittal plots. In most subjects, 25 cardiac cycles can be imaged in less than 25 seconds. As such, a very short pre-scan can reduce scan time considerably by allowing a wider acceptance window. We observe a minor sinusoidal fluctuation from 5 to 30 samples in same of the components of some of the subjects. This is consistent with the distribution of the

samples from end-expiration to end-inspiration, where a complete respiratory cycle typically lowers the error, while reducing or increasing the number of samples away from a complete cycle increases the error slightly. As the number of samples increases, the effect is reduced. A simple solution would be to monitor respiration in order to ensure that data from a complete number of respiratory cycles are used.

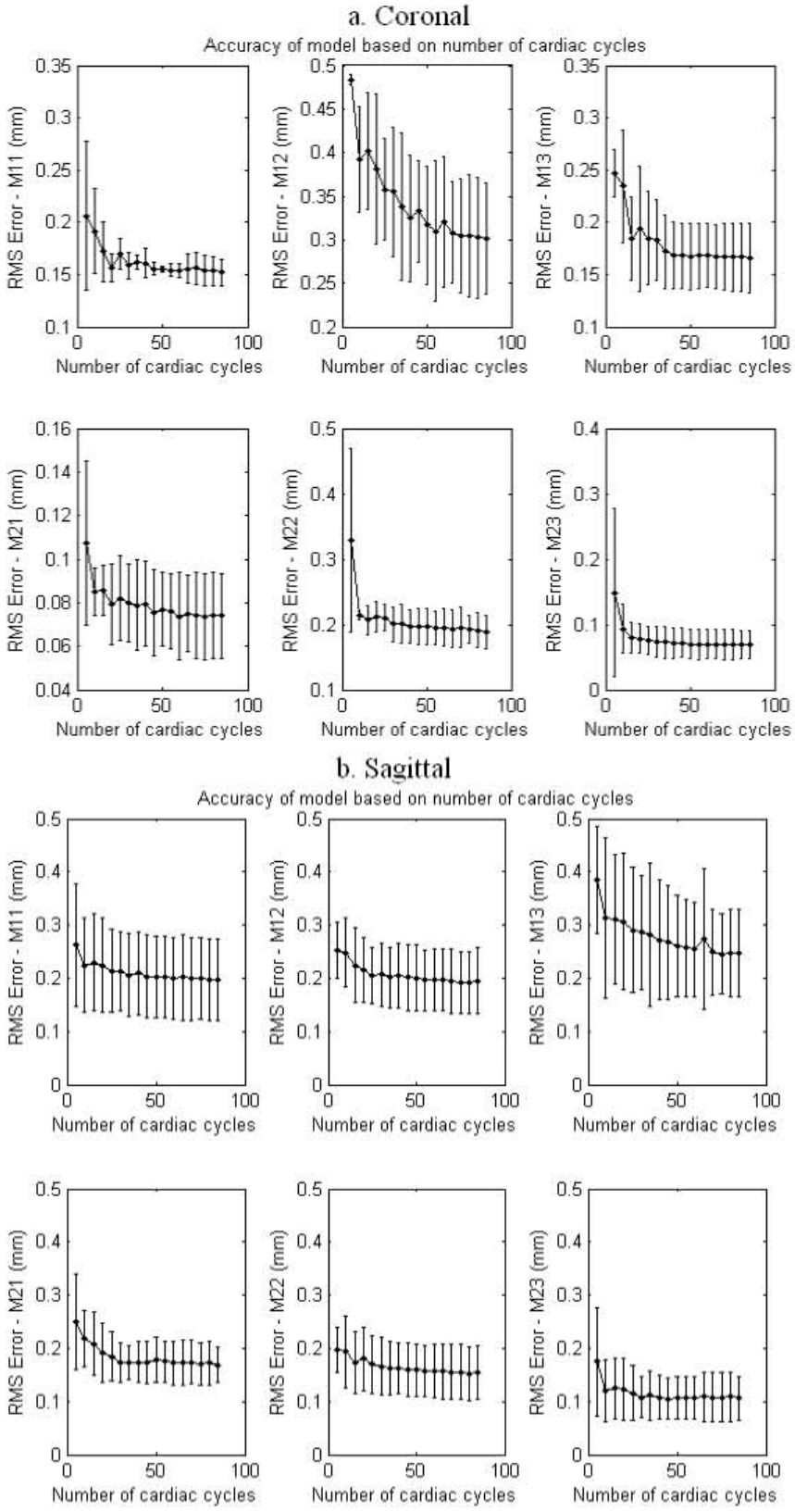

Figure 3.11: The RMS error (± standard deviation) of the different components of the model as a function of the number of cardiac cycles used to construct the model for (a) coronal images and b) sagittal images.

3.5 Discussion

Motion of the heart due to respiration is complex, and includes translation, rotation and deformation. In this study we investigated motion of the heart during free breathing in order to develop a model that could improve prospective motion correction in cardiac MRI. We have established that within subjects the pattern of motion due to respiration remains consistent. The inter-subject variation is not limited to a correction factor but also the amount of hysteresis and depth of breathing, underscoring the need for subject specific modelling. This study was performed with the subjects breathing freely since holding one's breath changes the respiratory patterns. Using a model constructed from one acquisition and testing it on a second provides evidence that the pattern of breathing does remain the same in a given subject.

It has been established that respiratory motion of the heart relative to diaphragm displacement can accurately be represented using an ellipse superimposed on a straight line and that the model can be constructed accurately within 25 cardiac cycles (~25 seconds). This model represents respiratory motion more accurately than a rigid model and a linear affine model.

For this model to be implemented in real time and prospectively correct respiratory motion, a distinction has to be made between inspiration and expiration. For this study, a positive gradient was taken as inspiration and a negative gradient as expiration. This approach works, but some errors occur at the ends due to the fact that the interval between measurements is about 700-900 ms. This problem can be overcome by using multiple navigators during the systolic period of the cardiac cycle (Burger et al., 2010) in order to distinguish between expiration and inspiration. Including multiple navigators will not increase the scan time since the navigators are executed in the systole where no image acquisition is performed.

The model matrix can then be used to correct for through plane motion in real time by adjusting the slice position before each echo is executed so that the slice that is excited and read out is positioned over the desired part of the heart. The in plane motion can be corrected during post processing, since the motion model, the navigator values and all the image data is available.

According to our results, the model should be precise enough for use in structural cardiac imaging. Non proton imaging such as sodium and potassium would benefit from motion

correction using the model since these tend to have extremely long scan times. With this model and prospective slice correction, the acceptance window with gated cardiac imaging can be increased from 5 mm to 10-20 mm or possibly even replace gating altogether.

In view of the results presented, the model could be used in coronary imaging. While it may be possible to combine the sagittal and coronal models into one three-dimensional model, this requires further investigation since acquisition of the two images may occur at significantly different time points. An alternative is to perform the process in 3D rather than 2D. Since a whole image needed to be acquired in 200-300 ms, it was not possible to perform the current study in three dimensions. Introducing accelerated image processing tools, that include parallel imaging, non-Cartesian imaging as well as compressed sensing and other under sampling strategies, make acquiring a 3D model with a sufficiently high resolution a realistic goal.

3.6 Conclusion

This study has demonstrated that a short pre-scan (~25s) can be used to construct an accurate subject specific model to predict heart position for any point on the heart based on navigator outputs during free breathing cardiac MRI. It has also been shown that this model offers a significant improvement over a linear affine model.

3.7 Acknowledgements

The authors would like to thank their colleagues at Imperial College, London, especially David Firmin and Jennifer Keegen. This study was funded by the South African Research Chairs Initiative of the Department of Science and Technology and National Research Foundation of South Africa, the Medical Research Council of South Africa, South Africa / Norway Research Collaboration Programme, University of Cape Town, and Siemens Medical Solutions South Africa.

4. Chapter 4

Applications of the control system

4.1 Abstract

When performing paediatric cardiac MRI acquisition, respiratory and subject motion need to be dealt with. In this chapter we describe how the control system was incorporated in a biofeedback technique that was developed by Jhooti et al. (2011), which visually displays the respiratory motion of the subject as the trajectory of an aeroplane. By including a control system in the feedback loop, the temporal resolution of the visual feedback is improved, reducing the jerky movement produced by periods where no navigator data is available.

4.2 Introduction

Recently there has been an increase in the number of children requiring cardiac MRI (Muthurangu et al. , 2005; (Razavi et al., 2003)), and six in 1000 newborn babies present with congenital heart disease (Hoffman and Kaplan, 2002). Motion poses a major problem in the acquisition of magnetic resonance images, especially in children (Brown et al., 2010). Children have to remain still in the scanner for up to an hour and breath holding is difficult for young subjects (Taylor et al., 1997, Taylor et al., 1999b). Sedation or general anaesthetics is generally necessary for children under the age of seven. Operant conditioning has been successfully implemented to encourage cooperation of children during MR imaging. (Slifer et al., 1993).

Respiratory gating during free breathing eliminates the need for breath holding, but typically reduces the respiratory efficiency to ~40% (Oshinski et al., 1996). Navigator biofeedback to guide free-breathing acquisition maintained image quality and increased the respiratory efficiency compared to conventional free-breathing acquisition in a study by Feuerlein et al. (2009). A fixed navigator acceptance window during acquisition was used in this study. Since most individuals showed respiratory drift toward expiration, subjects had to compensate by reducing inspiration to keep the end-expiratory position within the predefined window. This proved to be a problem for most of the subjects.

Jhooti et al. (2010) developed a continuously adaptive windowing strategy (CLAWS) (Jhooti 2010) that provides the fastest acquisition possible irrespective of changes in the respiratory pattern. This technique acquires a segment of k-space data during every acquisition window recording each time the diaphragm position prior to the acquisition window. For an image requiring *n* data segments, the algorithm essentially ensures that as soon as *n* diaphragm positions within the specified tolerance (i.e. 5 mm) have occurred, that *n* unique data segments have been acquired and the acquisition is terminated. Major benefits of this method include automatic window selection that effectively deals with respiratory drift.

CLAWS was further improved by adding respiratory biofeedback (rBF) to guide the subjects' breathing to ensure a more consistent end-expiratory position in order to improve the respiratory efficiency (Jhooti et al., 2011). The feedback is displayed visually to subjects during scanning in the form of a game. A moving object (cartoon aeroplane) represents the diaphragm position in the superior/inferior (SI) direction (figure 4.1). Other objects, such as loops, represent the gating window at end-expiration. The idea is to guide the aeroplane through the hoops at end-expiration to improve respiratory efficiency. The loops are not fixed and adjust in real time according to the subject's breathing pattern. Paediatric cardiac MRI can benefit greatly from this technique, which reduces scan time while simultaneously distracting and entertaining the child during the scan.

Figure 4.1: The position of the moving object (plane) reflects the superior/inferior motion of the diaphragm. Expiration decreases the altitude of the object and inspiration increases it. The loops represent the desired end-expiratory position.

Multiple navigators, with a repeat time of 100ms, were implemented during the delay time in each cardiac cycle in order to update the position of the moving object. The navigator values adjust the "altitude" of the moving object, where end-expiration represents the lowest "altitude" and end-inspiration the highest "altitude" of the plane, as shown in figure 4.1.

A limitation of the rBF method is that navigators are not acquired during the acquisition period when imaging is performed, resulting in a lag of approximately 400 ms during each cardiac cycle when no new diaphragm information is available to update the position of the plane on the visual display. This produces a jerky motion in the plane's motion trajectory, which makes it difficult to control resulting in a reduced respiratory efficiency. Figure 4.2 shows a schematic of the multiple navigators for one cardiac cycle and the period during the acquisition window when no navigator values are acquired. By integrating the control system (CS) developed previously into the rBF system, the missing diaphragm values during the acquisition window can be predicted using the model, resulting in a more accurate and smoother motion trajectory for the object in the visual display.

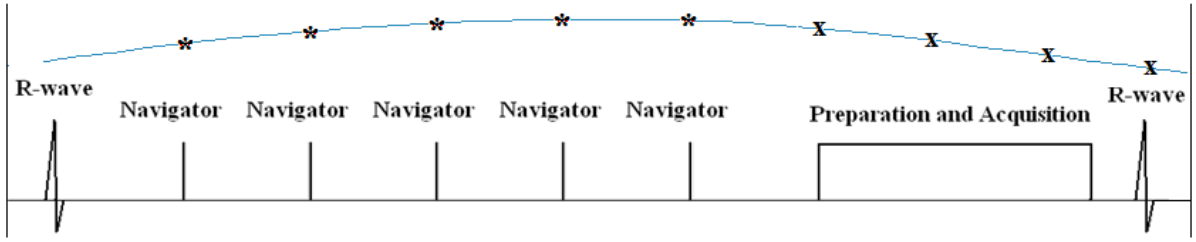

Figure 4.2: Single cardiac cycle with multiple navigators and an imaging segment near the end of the cardiac cycle. The curve above the ECG signal represents the diaphragm position. The asterisks denote navigator readings of the diaphragm position and the x's denote the intervals during the acquisition window when no navigator readings are available.

4.3 Methods

The rBF system receives the navigator value from the scanner via a User Datagram Protocol (UDP) socket. Jhooti et al (2011) have adapted the Image Calculation Environment (ICE) to transmit every navigator value received to a predefined IP address. The rBF system monitors this address via a network connection on an independent computer and adjusts the moving objects' altitude when a value is received.

A control system that predicts the upcoming diaphragm position during the imaging segment in cardiac MRI has been developed and previously described in detail (Burger et al., 2010). The control system was adapted and implemented in JAVA in order to fit into the rBF system, which was developed in a JAVA based environment. The control system required modification because in the rBF application the only information it receives are the navigator values. The number of navigators per cardiac cycle, the length of the acquisition window, the ECG trigger, and the pre-scan that is required to determine the breathing rate of the subject are not available to the control system.

The only alteration to the rBF setup is that the control system receives the navigator position from the scanner and transmits it to a new IP address. The rBF receive address has to be changed to this new address. The changes required in the rBF setup are shown in figure 4.3.

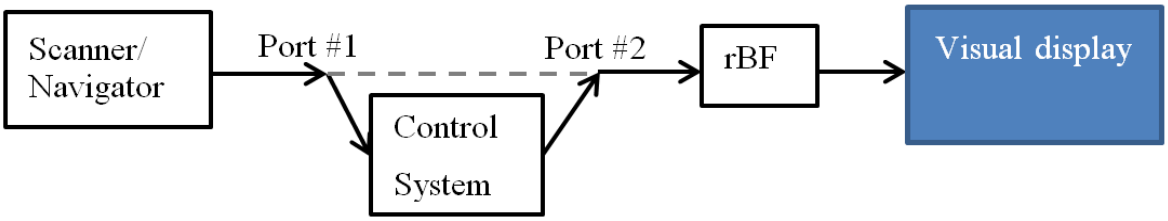

Figure 4.3: The control system receives the navigator value from the scanner and sends it to the respiratory biofeedback system which creates the visual display.

In order to determine the acceptance window for respiratory gating in the protocol, a scout image is typically acquired for 25 seconds. The navigator repeat time is 100 ms which results in 200 navigator samples. The control system uses this data to calculate the dominant frequency of breathing and the mean diaphragm position and displacement. The frequency is determined by zero padding the samples to 1024 and calculating the FFT. The initial breathing rate in the control system is set to the dominant frequency.

To overcome the problems related to the timing information that is not available to the control system, an algorithm that monitors the UDP socket was implemented (see figure 4.4). After the breathing rate and mean diaphragm position have been calculated, these initial conditions are set in the control system. The algorithm then waits for an input to the UDP socket. When the first input is received the navigator value is sent to the input port of the control system and via the control system to the output port that is connected to the rBF input. The algorithm then enters a loop in which it waits 102 ms for the next input. A 2 ms tolerance was added to the 100 ms repeat time of the multiple navigators. When an input is received within the 102 ms period, it is sent to the input of the control system and via the control system to the output port, but if no input is received within the 102 ms period the control system predicts the next diaphragm position, sends the value to the output port, and returns to the start of the loop. The loop will typically receive 4 to 5 navigator values followed by 3 to 4 predictions (see figure 4.2).

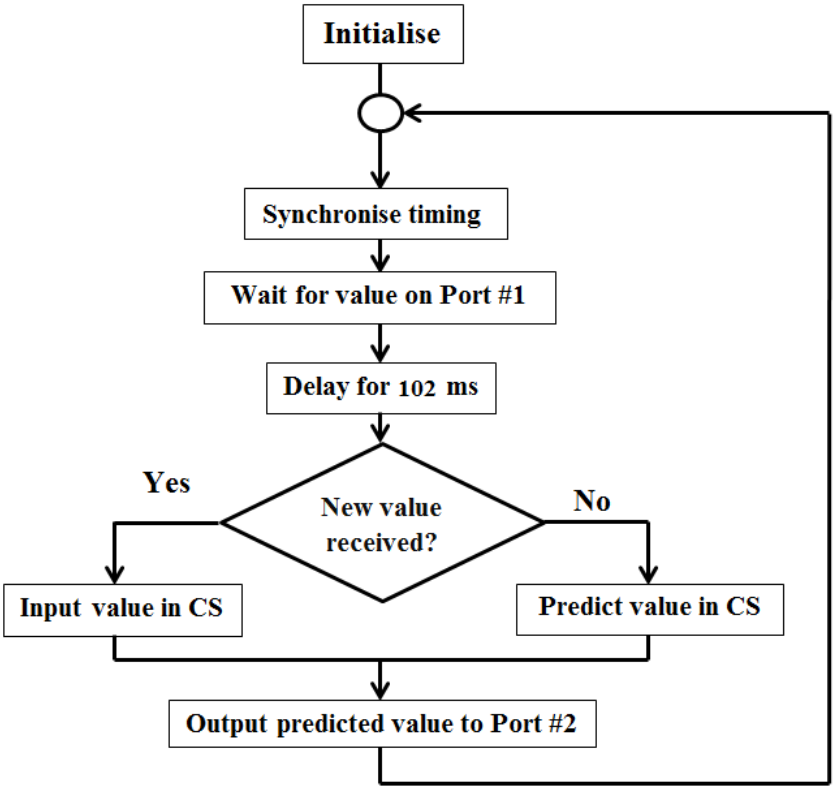

Figure 4.4: Flow chart of the algorithm that monitors the input port from the scanner. The abbreviation CS denotes the control system.

When the first navigator reading is again received after prediction it indicates the start of a new cardiac cycle. Since the control system functions periodically (T = 100ms) it needs to be synchronised with the physiological timing after each cardiac cycle. The cardiac cycle duration will hardly ever be an exact multiple of 100 ms. Further, the 2 ms tolerance also accumulates during the prediction period and will typically add 6 to 8 ms for a 300 to 400 ms acquisition window. This minor delay is of no concern during the particular cardiac cycle, since the effect of the delay is negligible (<0.01 mm), but can cause problems when allowed to accumulate. Equations 4.1 and 4.2 are used to correct the phase delay:

$$t_{cor} = 2 \times (samples\ predicted) + t_{extra} \tag{4.1}$$

$$f(kT_s) = \cos(akT_s + t_{cor}) \tag{4.2}$$

In order to validate the adapted control system, its performance was compared with that of the original control system (Burger et al., 2010). Real breathing patterns from eight subjects were used as input to both systems and the RMS errors of the predicted navigator outputs relative to the actual navigator measurements computed and compared for both systems. For

the validation five navigator samples were supplied to each of the two systems at 100ms intervals, followed by 440ms of no input. The phase correction is therefore included in the validation.

4.4 Results

For all subjects, the RMS errors of the predicted diaphragm positions compared to measured values are identical using the original and the adapted control systems. The adapted control system demonstrated a small non-significant drift (<0.01 mm) relative to the original system due to the 2 ms delay added during each prediction. The RMS errors of both systems are presented in table 4.1.

Table 4.1: Root mean squared (RMS) error of diaphragm predictions using the original and adapted control systems. Shown also is the range of diaphragm motion in the 8 volunteers.

Subject	1	2	3	4	5	6	7	8	Mean
Original RMS error (mm)	0.66	0.94	0.66	0.55	0.62	0.82	0.71	0.49	0.68
Adapted RMS error (mm)	0.66	0.94	0.66	0.55	0.62	0.82	0.71	0.49	0.68
Diaphragm range(mm)	14.25	15.58	11.80	15.21	16.16	17.27	13.38	12.53	14.52

Figure 4.5(a) shows an uncorrected feedback signal with jerky motion due to the absence of navigator values during the acquisition window, while (b) shows the feedback signal produced when using the control system in the rBF. Images (c) and (d) are close up views of a segment from (a) and (b), respectively, in order to emphasise the difference between the signals and the smoother trajectory that can be achieved with the control system added. In visual feedback generated without the control system (figure 4.6a) one can clearly see the sudden drop in the plane's altitude at the fifth frame, while the altitude of the plane decreases gradually in the visual feedback generated with the control system (figure 4.6b).

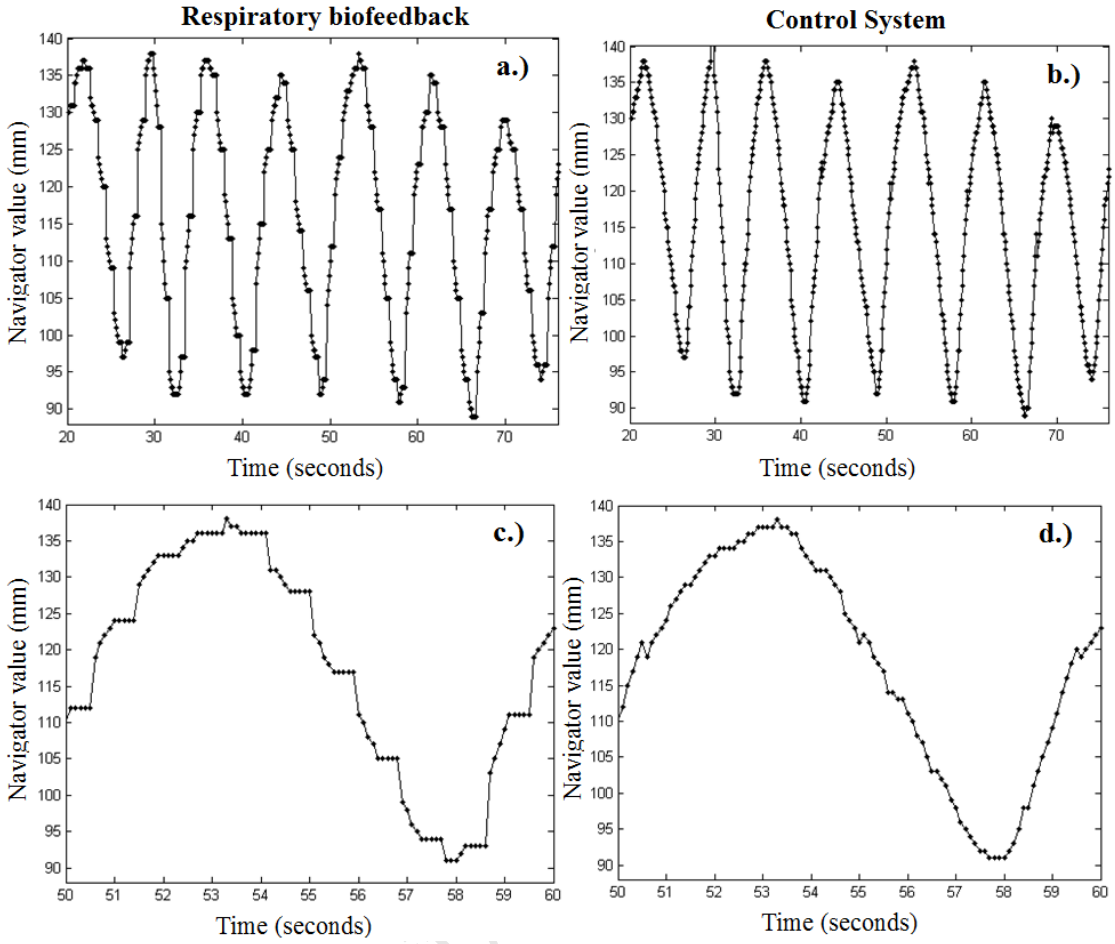

Figure 4.5: Comparison of the signal received by the respiratory biofeedback, (a) without the control system, and (b) with the control system. Images (c) and (d) are a closer view of a segment of (a) and (b), respectively.

4.5 Discussions

We have demonstrated that the adaptations that were made to the control system in order to permit its inclusion in rBF introduced no errors. The RMS errors of predicted diaphragm positions in eight subjects were identical using the adapted and original control systems, with mean RMS error 0.7 mm.

It has also been shown that the control system can successfully be implemented in a rBF system and produces a less jerky motion on the visual display. The system was validated using real breathing patterns of eight subjects.

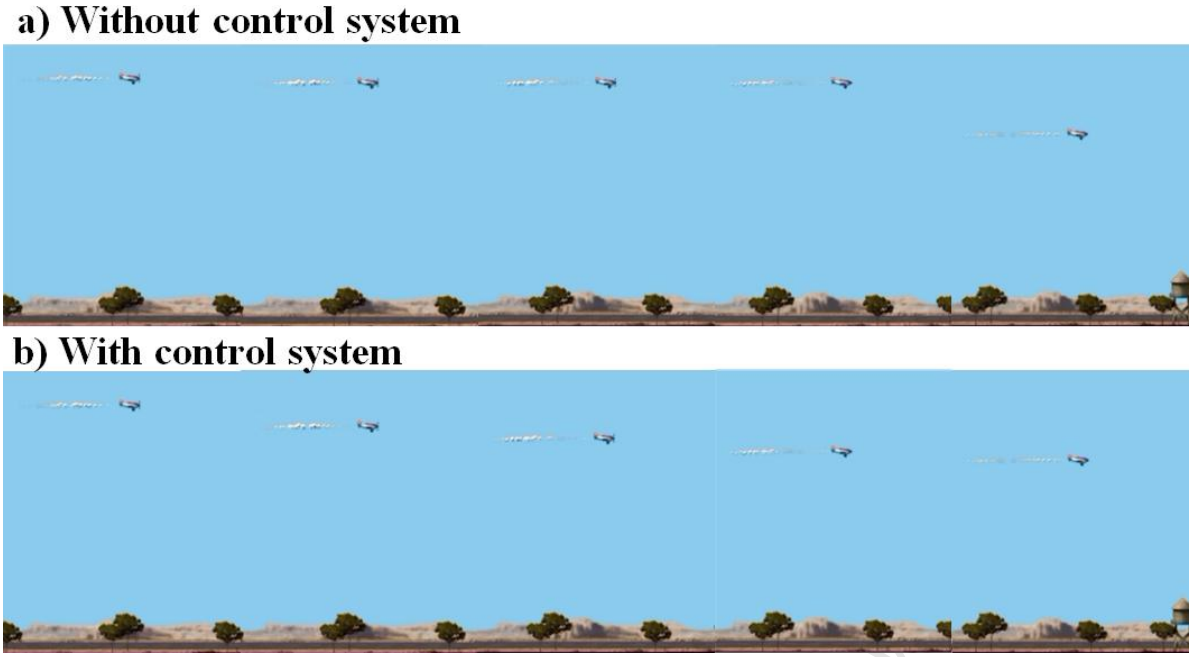

Figure 4.6: Five frames of the visual feedback produced a) without the control system; and b) with the control system.

The next step is to validate rBF with the control system *in vivo*. Comparing rBF with the control system with rBF alone will demonstrate whether adding the control system improves respiratory efficiency.

The times when outputs are received from the scanner can be monitored to establish whether the 2 ms tolerance is sufficient or whether it can be reduced if the output timing is proven stable.

4.6 Conclusion

Implementing a control system in rBF results in a smoother trajectory on the visual feedback, which could potentially increase respiratory efficiency by helping subjects to more easily control their breathing to ensure a consistent end-expiratory position. This could be especially valuable in paediatric cardiac MRI.

5. Chapter 5 Discussion

The control system used a cosine wave to model the respiratory motion of the heart. Using the respiratory traces of 8 subjects we demonstrated that the control system successfully predicts the diaphragm position in real time. The states of the control system are updated during each cardiac cycle to correct for variations in frequency and amplitude, as well as respiratory drift. The average RMS error of 0.68 mm is significantly smaller than the 5mm acceptance window typically used in respiratory gating.

The results of phantom experiments showed that the control system successfully updates the slice position on the scanner in real time. The quality of images acquired using the control system and respiratory gating were compared by evaluating the sharpness of the edges. The quality of the images acquired using the control system were significantly better for amplitudes of motion greater than 20 mm.

Images acquired *in vivo* from a single healthy volunteer using the control system and respiratory gating were of similar quality, but with a major difference in respiratory efficiency. The control system acquired the image with a 100% respiratory efficiency, whereas the gated sequence had a respiratory efficiency of 43%. Similar respiratory efficiencies were recorded during the phantom scans. A constant correction factor of 0.6 was used to adjust for differences between diaphragm and cardiac displacements for the *in vivo* image acquired using the control system. While this appears to be an appropriate correction factor for this particular subject, this may not always be true due to inter subject variation and the complex motion of the heart. A subject specific model of cardiac motion relative to diaphragm positions would yield improved slice following during the imaging segment.

While limited variation was observed in the breathing patterns within a subject, the inter-subject variation was not limited to a correction factor but also to the amount of hysteresis and depth of breathing, emphasizing the need for subject-specific modelling. The model was constructed using one acquisition and was tested on a second. The results show that respiratory motion of the heart relative to diaphragm displacement can accurately be represented using an ellipse superimposed on a straight line. For the elliptical model, the RMS errors of each transformation component were less than 0.5 mm and were significantly better than a linear non-rigid model for all the subjects.

The model matrix can then be used to correct for through plane motion in real time by adjusting the slice position before each echo is executed so that the slice that is excited and read out is positioned over the desired part of the heart. The in plane motion can be corrected during post processing, since the motion model, the navigator values and all the image data is available. By using this model with prospective motion correction the acceptance window of gated cardiac imaging can be increased to 10-20 mm or possibly even eliminated.

Finally, we successfully integrated the control system with a respiratory biofeedback system that visually displays the respiratory position of a subject in the MRI scanner using the trajectory of a plane's flight.

The adaptations made to the control system for it to be integrated with the respiratory biofeedback did not alter the accuracy of the system. The RMS errors of predicted diaphragm positions in eight subjects were identical using the adapted and original control systems, with mean RMS error 0.7 mm.

The system was validated using real breathing patterns of eight subjects and the visual display with the control system was much smoother than the display without it. The next step is to test the respiratory biofeedback with the control system *in vivo* to determine if the respiratory efficiency improves.

5.1 Limitations

A major limitation of this work was the absence of extensive *in* vivo validation. The control system was validated in only one healthy adult volunteer. Although, the subject specific model of respiratory motion was validated using real breathing patterns of 8 healthy subjects

that were acquired during short scans, the model was not implemented in the control system on the scanner and as such could not be validated during prolonged scanning, limiting the ability to explore the effects of factors such as respiratory drift on the model implementation. Extensive *in vivo* validation was not possible in the present study due to limited scanner access and the fact that customer sequences could not be loaded onto the local scanner because of delays related to the research licence agreement. All the scanner data presented in the thesis was acquired during an exchange visit to Royal Brompton Hospital, Imperial College London.

The current implementation of the control system predicts the positions of the diaphragm throughout the imaging segment, and then uses a constant correction factor to compute the corresponding positions of the heart in order to update the slice position in real time during the imaging segment. Since there is a lot of inter and intra subject variation in respiratory patterns, a constant correction factor is not optimal.

Respiratory motion during acquisition of the single shot images may affect the accuracy of the model. Although small, this motion will still affect image co-registration.

No significant respiratory drift was observed. Since the test series was performed 90 s after the reference series, large changes in mean breathing rate or bulk shift in position may not be well tested.

5.2 Future work

Future work should include extensive *in vivo* validation of the current implementation of the control system in healthy adult volunteers and in patients with cardiac disease. The subject specific model should also be implemented in the control system and validated *in* vivo in order to determine the improvements over a constant correction factor. By implementing the subject specific model of respiratory motion in the control system, a complete motion correction system can be developed for cardiac MRI that updates the slice position in real time throughout the imaging segment according to the subject's current breathing pattern and a model of the relative motion of the heart and diaphragm for that subject. In plane motion correction can also be applied retrospectively using the model and the navigator data acquired during the acquisition.

Respiratory biofeedback can be added to the above implementation, as this would assist subjects to maintain a constant breathing pattern, thus improving the accuracy of the model and the control system. Visual biofeedback is especially useful in children, who are also entertained and distracted by the "game".

By combining the models that were constructed using the sagittal and coronal images, a three dimensional model of the motion of the heart can be developed. The current setup would, however, double the time required to acquire the images needed to construct the model. Registering image data that may have been acquired at significantly different times in the respiratory cycle is also non-trivial. A possible solution to this problem is to incorporate compressed sensing, facilitating acquisition at acceleration factors of 4 (Li, 2011). This will enable two coronal and two sagittal images to be acquired per cardiac cycle as illustrated in figure 5.1. By combining four images acquired per cardiac cycle, a three dimensional model of the heart motion can be constructed within approximately 25 s.

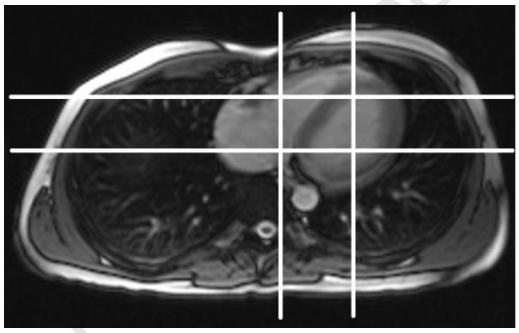

Figure 5.1: Transverse slice of the heart. White lines represent the slice positions required to construct a three dimensional model of respiratory cardiac motion.

6. Chapter 6
Conclusion

A prospective motion correction technique for cardiac- and respiratory-resolved MRI has been described and verified through simulation and phantom acquisitions and demonstrated *in vivo*. The results demonstrate that the control system accurately predicted the upcoming diaphragm position and corrected the slice position accordingly. The control system followed respiratory drift successfully by continuously updating the system throughout the scan. The control system produces better or equal image quality than respiratory gating using a gating window of 5mm. The control system completed the acquisitions with 100% respiratory efficiency compared to respiratory efficiencies below 50% for all the scans acquired using respiratory gating.

We have demonstrated that an ellipse superimposed on a straight line accurately describes the respiratory motion of the heart with significantly ($p < 0.05$) lower RMS errors than a linear model. The elliptical model presents a novel approach to respiratory motion modelling of the heart and accounts for both hysteresis and variation between subjects. Further we have established that the model can be constructed using a short pre scan of approximately 25 seconds so that it can be included in cardiac imaging prior to the sequence. Since the model construction is completely automated it requires no interaction from the operator.

Finally, we have applied the control system to real respiratory data to improve the temporal resolution in a visual respiratory biofeedback system. The result is a much smoother motion of the object representing the respiratory motion, making it easier for subjects to guide their breathing through the desired position. Paediatric MRI can benefit greatly from this application, since children struggle to stay still and to perform breath holding for cardiac imaging.

By combining all the elements presented here, a complete motion correction system can be developed for cardiac MRI that (1) predicts diaphragm positions throughout the imaging segment according to the subject's current breathing pattern, (2) uses a subject specific model of the relationship between cardiac and diaphragm positions to update the slice position in real time, and (3) provides visual feedback to the subject of their breathing to assist them in maintaining a consistent breathing pattern, which improves the accuracy of both the control system and the model in steps 1 and 2 above.

References

Alfidi R, Haaga J, El Yousef S (1982) Organs,"Philos. Trans. R. Soc. Lend. B289: 425. Radiology 143:175-181.

Atkinson DJ, Edelman R (1991) Cineangiography of the heart in a single breath hold with a segmented turboFLASH sequence. Radiology 178:357-360.

Bailes D, Gilderdale D, Bydder G, Collins A, Firmin D (1985) Respiratory ordered phase encoding (ROPE): a method for reducing respiratory motion artefacts in MR imaging. Journal of computer assisted tomography 9:835.

Bernstein MA, King KE, Zhou XJ, Fong W (2005) Handbook of MRI pulse sequences. Medical Physics 32:1452.

Bogren H, Lantz B, Miller R, Mason D (1977) Effect of respiration on cardiac motion determined by cineangiography. Implications concerning three-dimensional heart reconstruction using computer tomography. Acta radiologica: diagnosis 18:609.

Botnar RM, Stuber M, Danias PG, Kissinger KV, Manning WJ (1999) A fast 3D approach for coronary MRA. Journal of Magnetic Resonance Imaging 10:821-825.

Brown TT, Kuperman JM, Erhart M, White NS, Roddey JC, Shankaranarayanan A, Han ET, Rettmann D, Dale AM (2010) Prospective motion correction of high-resolution magnetic resonance imaging data in children. NeuroImage 53:139-145.

Buliev IG, Badea CT, Kolitsi Z, Pallikarakis N (2003) Estimation of the heart respiratory motion with applications for cone beam computed tomography imaging: a simulation study. Information Technology in Biomedicine, IEEE Transactions on 7:404-411.

Burger IH, Meintjes EM, Keegen J, D. F (2010) Prospective Diaphragm Position Prediction for Cardiac MRI using multiple navigators. In: ISMRM Motion correction workshop Kitzbühel, Tyrol, Austria.

Danias P, Stuber M, Botnar R, Kissinger K, Chuang M, Manning W (1998) Navigator assessment of breath-hold duration: impact of supplemental oxygen and hyperventilation. American journal of Roentgenology 171:395-397.

Danias P, Stuber M, Botnar R, Kissinger K, Edelman R, Manning W (1999) Relationship between motion of coronary arteries and diaphragm during free breathing: lessons from real time MR imaging. American journal of Roentgenology 172:1061-1065.

Danias PG, McConnell MV, Khasgiwala VC, Chuang ML, Edelman RR, Manning WJ (1997) Prospective navigator correction of image position for coronary MR angiography. Radiology 203:733.

Ehman R, McNamara M, Pallack M, Hricak H, Higgins C (1984) Magnetic resonance imaging with respiratory gating: techniques and advantages. American journal of Roentgenology 143:1175-1182.

Ehman RL, Felmlee J (1989) Adaptive technique for high-definition MR imaging of moving structures. Radiology 173:255-263.

Feinberg DA, Rofsky NM, Johnson G (1995) Multiple breath-hold averaging (mba) method for increased snr in abdominal mri. Magnetic resonance in medicine 34:905-909.

Feuerlein S, Klass O, Pasquarelli A, Brambs HJ, Wunderlich A, Duerk JL, Aschoff AJ, Hoffmann MHK (2009) Coronary MR imaging: navigator echo biofeedback increases navigator efficiency—initial experience. Academic radiology 16:374-379.

Firmin D, Keegan J (2001) Navigator echoes in cardiac magnetic resonance. Journal of Cardiovascular Magnetic Resonance 3:183-193.

Franklin GF, Powell JD, Workman M (1998) Digital Control of Dynamic Systems.

Gatehouse PD, Firmin DN (2000) The cardiovascular magnetic resonance machine: hardware and software requirements. Herz 25:317-330.

Gene F. Franklin JDP, Michael Workman, J David Powel, Workman M (1997) Digital control of dynamicSystems. In: Digital control of dynamicSystems.

Haacke EM, Brown RW, Thompson MR, Venkatesan R (1999) Magnetic resonance imaging: physical principles and sequence design (First edition) Wiley-Liss New York:.

Hashemi RH, Bradley WG (1997) MRI: the basics (Second edition).

Herron R (2008) Connectivity analysis of brain function in children with foetal alcohol spectrum disorder and control children during number processing.

Hess AT, Dylan Tisdall M, Andronesi OC, Meintjes EM, van der Kouwe AJW (2011) Real time motion and B0 corrected single voxel spectroscopy using volumetric navigators. Magn Reson Med.

Higgins C, Byrd B, McNamara M, Lanzer P, Lipton M, Botvinick E, Schiller N, Crooks L, Kaufman L (1985) Magnetic resonance imaging of the heart: a review of the experience in 172 subjects. Radiology 155:671-679.

Higgins CB (2000) Cardiac Imaging1. Radiology 217:4-10.

Hinks RS (1988) Monitored echo gating for the reduction of motion artifacts. Google Patents.

Hinshaw WS (1976) Image formation by nuclear magnetic resonance: The sensitive-point method. Journal of Applied Physics 47:3709-3721.

Hoffman JIE, Kaplan S (2002) The incidence of congenital heart disease. Journal of the American College of Cardiology 39:1890.

Holland AE, Goldfarb JW, Edelman RR (1998) Diaphragmatic and cardiac motion during suspended breathing: preliminary experience and implications for breath-hold MR imaging. Radiology 209:483.

Innes J, De Cort S, Kox W, Guz A (1993) Within-breath modulation of left ventricular function during normal breathing and positive-pressure ventilation in man. The Journal of Physiology 460:487.

Jahnke C, Paetsch I, Achenbach S, Schnackenburg B, Gebker R, Fleck E, Nagel E (2006) Coronary MR Imaging: Breath-hold Capability and Patterns, Coronary Artery Rest Periods, and ß-Blocker Use1. Radiology 239:71-78.

Jhooti P, Haas T, Kawel N, Bremerich J, Keegan J, Scheffler K (2011) Use of respiratory biofeedback and CLAWS for increased navigator efficiency for imaging the thoracic aorta. Magnetic resonance in medicine.

Jhooti P, Keegan J, Firmin D (2010) A fully automatic and highly efficient navigator gating technique for high-resolution free-breathing acquisitions: Continuously adaptive windowing strategy. Magnetic resonance in medicine 64:1015-1026.

Jhooti P, Keegan J, Gatehouse P, Collins S, Rowe A, Taylor A, Firmin D (1999) 3D coronary artery imaging with phase reordering for improved scan efficiency. Magnetic resonance in medicine 41:555-562.

Keele CN, E. (1965) Samson Wright's applied physiology.

Klein A, Kroon DJ, Hoogeveen Y, Schultze Kool LJ, Renema WKJ, Slump CH (2011) Multimodal image registration by edge attraction and regularization using a B-spline grid. SPIE.

Kozerke S, Hasenkam JM, Nygaard H, Paulsen PK, Pedersen EM, Boesiger P (2001) Heart Motion-adapted MR Velocity Mapping of Blood Velocity Distribution Downstream of Aortic Valve Prostheses: Initial Experience1. Radiology 218(2):548-555.

Kozerke S, Scheidegger MB, Pedersen EM, Boesiger P. (1999) Heart motion adapted cine phase- contrast flow measurements through the aortic valve. Magnetic Resonance in Medicine 42(5):970-978.

Lanzer P, Barta C, Botvinick E, Wiesendanger H, Modin G, Higgins C (1985) ECG-synchronized cardiac MR imaging: method and evaluation. Radiology 155:681-686.

Li D (2011) An improved CS applied for MRI. International Journal of Research and Reviews in Soft and Intelligent Computing (IJRRSIC) 1.

Li D, Kaushikkar S, Haacke EM, Woodard PK, Dhawale PJ, Kroeker RM, Laub G, Kuginuki Y, Gutierrez FR (1996) Coronary arteries: three-dimensional MR imaging with retrospective respiratory gating. Radiology 201:857.

Liu YL, Riederer SJ, Rossman PJ, Grim RC, Debbins JP, Ehman RL (1993) A monitoring, feedback, and triggering system for reproducible breath-hold MR imaging. Magnetic resonance in medicine 30:507-511.

Manke D, Nehrke K, Börnert P, Rösch P, Dössel O (2002a) Respiratory motion in coronary magnetic resonance angiography: a comparison of different motion models. Journal of Magnetic Resonance Imaging 15:661-671.

Manke D, Rosch P, Nehrke K, Bornert P, Dossel O (2002b) Model evaluation and calibration for prospective respiratory motion correction in coronary MR angiography based on 3-D image registration. Medical Imaging, IEEE Transactions on 21:1132-1141.

Marks B, Mitchell DG, Simelaro JP (1997) Breath-holding in healthy and pulmonary-compromised populations: Effects of hyperventilation and oxygen inspiration. Journal of Magnetic Resonance Imaging 7:595-597.

Martini FH, Bartholomew EF (2007) Essentials of Anatomy & Physiology (4th Edition), Pearson Education

McCarthy RM, Shea SM, Deshpande VS, Green JD, Pereles FS, Carr JC, Finn JP, Li D (2003) Coronary MR Angiography: True FISP Imaging Improved by Prolonging Breath Holds with Preoxygenation in Healthy Volunteers1. Radiology 227:283.

McConnell M, Khasgiwala V, Savord B, Chen M, Chuang M, Edelman R, Manning W (1997) Comparison of respiratory suppression methods and navigator locations for MR coronary angiography. American journal of Roentgenology 168:1369-1375.

McLeish K, Hill DLG, Atkinson D, Blackall JM, Razavi R (2002) A study of the motion and deformation of the heart due to respiration. Medical Imaging, IEEE Transactions on 21:1142-1150.

Nehrke K, Börnert P (2005) Prospective correction of affine motion for arbitrary MR sequences on a clinical scanner. Magnetic resonance in medicine 54:1130-1138.

Nehrke K, Börnert P, Manke D, Böck JC (2001) Free-breathing Cardiac MR Imaging: Study of Implications of Respiratory Motion—Initial Results1. Radiology 220:810-815.

Oshinski JN, Hofland L, Mukundan S, Dixon WT, Parks WJ, Pettigrew RI (1996) Two-dimensional coronary MR angiography without breath holding. Radiology 201:737.

Parish TB, Fieno DS, Fitzgerald SW, Judd RM (1997) Theoretical basis for sodium and potassium MRI of the human heart at 1.5 T. Magnetic resonance in medicine 38:653-661.

Pauly J, Nishimura D, Macovski A (1989) A k-space analysis of small-tip-angle excitation. Journal of Magnetic Resonance (1969) 81:43-56.

Razavi RS, Hill DLG, Muthurangu V, Miquel ME, Taylor AM, Kozerke S, Baker EJ (2003) Three-dimensional magnetic resonance imaging of congenital cardiac anomalies. Cardiology in the Young 13:461-465.

Rosamond W, Flegal K, Furie K, Go A, Greenlund K, Haase N, Hailpern SM, Ho M, Howard V, Kissela B (2008) Heart disease and stroke statistics—2008 update. Circulation 117:e25-e146.

Sachs TS, Meyer CH, Hu BS, Kohli J, Nishimura DG, Macovski A (1994) Real-time motion detection in spiral MRI using navigators. Magnetic resonance in medicine 32:639-645.

Sakuma H, Kawada N, Kubo H, Nishide Y, Takano K, Kato N, Takeda K (2001) Effect of breath holding on blood flow measurement using fast velocity encoded cine MRI. Magnetic resonance in medicine 45:346-348.

Scott AD, Keegan J, Firmin DN (2009) Motion in Cardiovascular MR Imaging1. Radiology 250:331-351.

Serfaty JM, Yang X, Aksit P, Quick HH, Solaiyappan M, Atalar E (2000) Toward MRI-guided coronary catheterization: Visualization of guiding catheters, guidewires, and anatomy in real time. Journal of Magnetic Resonance Imaging 12:590-594.

Shechter G, Ozturk C, Resar JR, McVeigh ER (2004) Respiratory motion of the heart from free breathing coronary angiograms. Medical Imaging, IEEE Transactions on 23:1046-1056.

Silverthorn D (2010) Human Physiology, an integrated approach.

Slifer KJ, Cataldo MF, Cataldo MD, Llorente AM, Gerson A (1993) Behavior analysis of motion control for pediatric neuroimaging. Journal of applied behavior analysis 26:469.

Spottiswoode B (2006) Towards automating cine DENSE MRI image analysis: segmentation, tissue tracking and strain computation.

Steiner R, Bydder G, Selwyn A, Deanfield J, Longmore D, Klipsten R, Firmin D (1983) Nuclear magnetic resonance imaging of the heart. Current status and future prospects. British heart journal 50:202-208.

Stuber M, Botnar RM, Danias PG, Kissinger KV, Manning WJ (1999) Submillimeter Three-dimensional Coronary MR Angiography with Real time Navigator Correction: Comparison of Navigator Locations1. Radiology 212:579.

Stuber M, Botnar RM, Spuentrup E, Kissinger KV, Manning WJ (2001) Three-dimensional high-resolution fast spin-echo coronary magnetic resonance angiography. Magnetic resonance in medicine 45:206-211.

Taylor AM, Jhooti P, Wiesmann F, Keegan J, Firmin DN, Pennell DJ (1997) MR navigator-echo monitoring of temporal changes in diaphragm position: Implications for MR coronary angiography. Journal of Magnetic Resonance Imaging 7:629-636.

Taylor AM, Keegan J, Jhooti P, Firmin DN, Pennell DJ (1999a) Calculation of a subject-specific adaptive motion-correction factor for improved real time navigator echo-gated magnetic resonance coronary angiography. Journal of Cardiovascular Magnetic Resonance 1:131-138.

Taylor AM, Keegan J, Jhooti P, Gatehouse PD, Firmin DN, Pennell DJ (1999b) Differences between normal subjects and patients with coronary artery disease for three different MR coronary angiography respiratory suppression techniques. Journal of Magnetic Resonance Imaging 9:786-793.

Van De Graaff K (2002) Human Anatomy: McGraw-Hill.

van der Kouwe AJW, Benner T, Dale AM (2006) Real time rigid body motion correction and shimming using cloverleaf navigators. Magn Reson Med 56:1019-1032.

Wang Y, Christy PS, Korosec FR, Alley MT, Grist TM, Polzin JA, Mistretta CA (1995a) Coronary MRI with a respiratory feedback monitor: the 2D imaging case. Magnetic resonance in medicine 33:116-121.

Wang Y, Ehman RL (2000) Retrospective adaptive motion correction for navigator-gated 3D coronary MR angiography. Journal of Magnetic Resonance Imaging 11:208-214.

Wang Y, Riederer SJ, Ehman RL (1995b) Respiratory motion of the heart: kinematics and the implications for the spatial resolution in coronary imaging. Magnetic resonance in medicine 33:713-719.

Weissler AM, Harris WS, Schoenfeld CD (1968) Systolic time intervals in heart failure in man. Circulation 37:149-159.

Welch EB, Manduca A, Grimm RC, Ward HA, Jack Jr CR (2002) Spherical navigator echoes for full 3D rigid body motion measurement in MRI. Magn Reson Med 47:32-41.

White N, Roddey C, Shankaranarayanan A, Han E, Rettmann D, Santos J, Kuperman J, Dale A (2010) PROMO: Real-time prospective motion correction in MRI using image-based tracking. Magn Reson Med 63:91-105.

Zhang S, Rafie S, Chen Y, Hillenbrand CM, Wacker FK, Duerk JL, Lewin JS (2006) In vivo cardiovascular catheterization under real-time MRI guidance. Journal of Magnetic Resonance Imaging 24:914-917.

Appendix: Control theory, comprehensive derivation of the equations used from theory:

The continuous state space model is described by:

$$\dot{x} = Fx + Bu \tag{A.1}$$

$$y = Cx + D \tag{A.2}$$

The mathematical model for the system is:

$$f(kT_s) = \sin(akT_s), \tag{A.3}$$

where the frequency of the breathing/oscillation:

$$a = 2\Pi\omega \tag{A.4}$$

and the sample rate is:

$$T_s = period(seconds) \tag{A.5}$$

The Laplace transform of equation a.3 is:

$$F(s) = \frac{a}{s^2 + a^2}, \tag{A.6}$$

And the transfer function is:

$$F(s) = \frac{y(s)}{u(s)} \tag{A.7}$$

$$y(s)s^2 = -y(s)a^2 + u(s)a \tag{A.8}$$

$$u = 0 \tag{A.9}$$

$$y(s)s^2 = -y(s)a^2 \tag{A.10}$$

$$\ddot{y} = -ya^2 \tag{A.11}$$

, now we set:

$$\ddot{y} = \dot{x}_1 \tag{A.12}$$

and:

$$\dot{y} = \dot{x}_2 \tag{A.13}$$

, since the derivatives give

$$\dot{y} = x_1 \tag{A.14}$$

and

$$x_2 = y \tag{A.15}$$

we can say

$$\dot{x}_1 = \ddot{y} = -ya^2 = -a^2 x_2 \tag{A.16}$$

and

$$\dot{x}_2 = x_1 \tag{A.17}$$

giving

$$\begin{bmatrix} \dot{x}_1 \\ \dot{x}_2 \end{bmatrix} = \begin{bmatrix} 0 & -a^2 \\ 1 & 0 \end{bmatrix} \begin{bmatrix} x_1 \\ x_2 \end{bmatrix} \tag{A.18}$$

and since:

$$\dot{x} = Fx + Bu\,, \tag{A.19}$$

$$u = 0 \tag{A.20}$$

and

$$\dot{x} = Fx \tag{A.21}$$

we can say that

$$F = \begin{bmatrix} 0 & -a^2 \\ 1 & 0 \end{bmatrix} \tag{A.22}$$

The discrete state space model is described as:

$$x(k+1) = \Phi x(k) + \Gamma u(k) \tag{A.23}$$

$$y(k) = Hx(k) \tag{A.24}$$

And by substituting

$$\Phi = e^{FT_s} \approx I + (FT_s) + \frac{(FT_s)^2}{2!} + \frac{(FT_s)^3}{3!} \approx I + (FT_s) \tag{A.25}$$

$$\Gamma = \int_0^T e^{F\eta} \partial\eta \cdot G = F^{-1} e^{F\eta} \Big|_0^T G = F^{-1}(\Phi - I)G \tag{A.26}$$

we get that:

$$\Phi = \begin{bmatrix} 1 & -a^2 T \\ T & 1 \end{bmatrix} \tag{A.27}$$

and since we want to output the current state, which is x_1, we set:

$$y = x_1 \tag{A.28}$$

and since

$$y = Hx \tag{A.29}$$

we get

$$H = \begin{bmatrix} 1 & 0 \end{bmatrix} \tag{A.30}$$

$$\Phi = \begin{bmatrix} 1 & -a^2T \\ T & 1 \end{bmatrix} \tag{A.31}$$

Next we place the poles (the poles determine whether the system follows the model more closely or the plant)

$$z_{est} = placed\ poles = real \pm j\ imaginary = z_{estR} \pm jz_{estI} \tag{A.32}$$

and factorizing this gives

$$(Z - Z_{estR} - jZ_{estI})(Z - Z_{estR} + jZ_{estI}) \tag{A.33}$$

$$Z^2 - Z_{estR}Z + jZ_{estI}Z - Z_{estR}Z + {Z_{estR}}^2 - jZ_{estR}Z_{estI} - jZ_{estI}Z + jZ_{estI}Z_{estR} + {Z_{estI}}^2 \tag{A.34}$$

$$Z^2 + 2Z_{estR}Z + {Z_{estR}}^2 + {Z_{estI}}^2 \tag{A.35}$$

$$Z^2 - Z_{est1}Z + Z_{est2} \tag{A.36}$$

$$Z_{est1} = -2Z_{estR} \tag{A.37}$$

$$Z_{est2} = {Z_{estR}}^2 + {Z_{estI}}^2 \tag{A.38}$$

$$Z^2 - z_{est1}Z + z_{est2} \tag{A.39}$$

We know that:

$$\left|ZI - \varphi + L_p H\right|, \tag{A.40}$$

by substituting Φ and H gives

$$(Z + L_{p1} - 1)(Z - 1) - (L_{p2} - T)(a^2 T) = 0 \tag{A.41}$$

$$Z^2 + (L_{p1} - 2)Z + (1 - L_{p1}) + a^2 T^2 - L_{p2} a^2 T = 0 \tag{A.42}$$

then solve for L_p:

$$(L_{p1} - 2) = -z_{est1} \tag{A.43}$$

$$L_{p1} = -z_{est1} + 2 \tag{A.44}$$

$$(1 - L_{p1}) + a^2 T^2 - L_{p2} a^2 T = z_{est2} \tag{A.45}$$

$$L_{p2} = \frac{a^2 T^2 - z_{est2} + 1 - L_{p1}}{a^2 T} \tag{A.46}$$